



Uncovering the important role of transverse acoustic phonons in the carrier-phonon scattering in silicon

Qiao-Lin Yang ^{1,2} Wu Li,³ Zhi Wang ^{2,4} Fan-long Ning,^{1,5,6,*} and Jun-Wei Luo^{2,4,†}

¹*School of Physics and Zhejiang Province Key Laboratory of Quantum Technology and Device, Zhejiang University, Hangzhou 310027, China*

²*State Key Laboratory of Superlattices and Microstructures, Institute of Semiconductors, Chinese Academy of Sciences, Beijing 100083, China*

³*Eastern Institute for Advanced Study, Eastern Institute of Technology, 315200 Ningbo, China*

⁴*Center of Materials Science and Optoelectronics Engineering, University of Chinese Academy of Sciences, Beijing 100049, China*

⁵*State Key Laboratory of Silicon and Advanced Semiconductor Materials, Zhejiang University, Hangzhou 310027, China*

⁶*Collaborative Innovation Center of Advanced Microstructures, Nanjing University, Nanjing 210093, China*



(Received 15 November 2023; revised 29 February 2024; accepted 11 March 2024; published 28 March 2024)

Carrier mobility is an essential parameter of semiconductors, characterizing how quickly carriers can move in a material when driven by an external electric field. Because electron-phonon (e-ph) scattering limits the room-temperature carrier mobility in high-quality semiconductors, understanding the mechanisms of interaction between carriers and phonons at the microscopic level is vital to investigate the transport properties, especially in nanoelectronic devices. Here, we reproduce the experimentally measured electron and hole mobility in silicon (Si) over a wide temperature range without relying on adjustable parameters by performing the first-principles calculations. By decomposition of the first-principles calculation-predicted e-ph scattering into the contributions from different phonon modes and electronic valleys, we show that the transverse acoustic (TA) phonon mode has a comparable contribution to the longitudinal acoustic (LA) phonon mode in scattering of both electrons and holes on limiting the carrier mobilities in Si. This is in striking contrast with the common sense that the TA mode is negligible based on the classical e-ph interaction modes. We unravel that the neglect of TA scattering is due to the substantial underestimation of the shear deformation potential (associated with the TA mode) with respect to the dilation deformation potential (associated with the LA mode). We also find that the transverse optical (TO) phonon mode, rather than the conventionally presumed longitudinal optical (LO) and LA modes, provides the leading scattering channel (accounting for 58%) in *f*-type intervalley scattering and the LO mode is dominant over the LA mode in *g*-type intervalley scattering for electrons in Si. These findings illustrate why the technology computer-aided design device simulation loses the predictive capability, although it is possible to obtain reasonable results using adjustable parameters based on the incorrect physics models. It calls for a revisit of the mechanisms underlying the carrier mobility in semiconductors.

DOI: [10.1103/PhysRevB.109.125203](https://doi.org/10.1103/PhysRevB.109.125203)

I. INTRODUCTION

Carrier-phonon scattering has been widely investigated over the past seven decades [1,2] since it limits room-temperature carrier mobility, which is an essential property of the response of semiconductor quantifying carriers to the external electric field and thus governs the performance of the device [3]. Properly Understanding the microscopic mechanisms of carrier-phonon scattering is, therefore, a necessary foundation for predicting instead of fitting (currently adopted) and enhancing the carrier transport properties in nanoscale semiconductor devices. Carrier-phonon scattering is tradition-

ally described by classical phenomenological models [1,2,4–7]. Specifically, Shockley and Bardeen [1,2] introduced the deformation potential theory (DPT) to describe carrier-phonon scattering in which the acoustic (AC)-phonon-limited scattering of carriers (electrons and holes) is related to the lattice-strain-induced local shift of the valence and conduction band edges due to atomic displacements accompanying the AC phonons. Herring and Vogt [4] extended DPT to the optical (OP) phonons, giving rise to nonpolar OP deformation potential (ODP) scattering. In nonpolar semiconductors such as group-IV elemental materials of C, Si, Ge, and Sn, AC deformation potential (ADP) scattering often dominates over ODP scattering [6,7]. In polar semiconductors such as group-III–V and II–VI compounds, Fröhlich [5], however, demonstrated that the scattering of carriers is mainly caused by electrical dipoles generated by the out-of-phase

*ningfl@zju.edu.cn

†jwluo@semi.ac.cn

displacement of the charged ions around their equilibrium position resulting from the longitudinal optical (LO) phonons.

To describe how strain affects the band structure, DPT [1,2] based on the first-order perturbation theory introduces a perturbation Hamiltonian $H(\varepsilon, n\mathbf{k}) = \sum_{\alpha,\beta=1}^3 D_{\alpha\beta}\epsilon_{\alpha\beta}$, where the indexes α and β denote the Cartesian direction (x, y, z), and $D_{\alpha\beta}$ and $\epsilon_{\alpha\beta}$ refer to the deformation potential constants and phonon-induced crystal deformation tensor, respectively. The number of independent constants $D_{\alpha\beta}$ is determined by the symmetry of the Brillouin zone (BZ) at the point \mathbf{k} . For instance, the homogenous deformation of a crystal induced by long-wavelength AC phonons can be described by the symmetrical second-rank deformation tensor $\{\epsilon_{\alpha\beta}\}$, and thus, the interaction Hamiltonian between AC phonons and electrons at the extremum of the conduction band at the point $k = 0$ (at which the second-rank tensor has only one independent component) can be defined as $H_{el} = D_{ac} \cdot \text{div } \mathbf{u}(\mathbf{r})$ [$\text{div } \mathbf{u}(\mathbf{r}) = \sum_{\alpha} \epsilon_{\alpha\alpha} = \Delta V/V$], where $\mathbf{u}(\mathbf{r})$ is the displacement vector of lattice vibrations caused by AC phonons and D_{ac} is the deformation potential constant. In this case, the perturbing potential only applies to longitudinal acoustic (LA) phonons because transverse acoustic (TA) phonons produce no changes to the lattice spacing in the first order [3,8]. However, if the cubic crystal has an off-center extreme in the conduction band (e.g., the conduction band extremum of Si and Ge are not located at the Γ point but at the Δ and L points, respectively), the symmetry of the BZ at these non- Γ points is lower than the symmetry of the crystal, resulting in the second-rank strain tensor having two independent components. The additional component corresponds to shear deformations, allowing the scattering of electrons by TA phonons [9]. However, Hamaguchi [6] illustrated that the contribution of TA phonons to electron scattering is negligible since the TA deformation potential is much smaller than the LA deformation potential, although TA phonon-assisted scattering of the electron is allowed by symmetry in Si. It leads to much of the literature and textbooks [3,6–8,10–12] having simply neglected the contribution of the TA mode in electron-phonon (e-ph) scattering and even in hole-phonon scattering. However, recent first-principles calculations have evidenced the significant role of the TA mode in carrier transport. For instance, Li *et al.* [13] showed that TA phonons play an equally important role to LA and LO phonons in the scattering of electrons in Si. Fischetti and Laux [14] found that the TA deformation potential should be one order of magnitude stronger than the dilation deformation potential in both Si and Ge by fitting simultaneously both the electron and hole mobilities to experimental values. These clues suggest that it is necessary to revisit the e-ph interactions in semiconductors.

Notice that the deformation potential constants utilized in DPT are usually treated as adjustable parameters to reproduce experimentally measured mobility [14]. Generally, the solutions of fitting these phenomenological methods to experimental mobilities are nonunique. One may obtain incorrect deformation potentials by an accident agreement [4,15]. For instance, in indirect band gap semiconductors such as Si and Ge, multivalley and degenerate bands of electrons involve numerous types of deformation potentials, leading to multiple sets of these deformation potential constants, giving rise to the same experimental value of carrier mobility. An

isotropic model is frequently employed to simplify the real complex band structure, and a single effective deformation potential constant is used to estimate carrier mobilities [14,16], which mixes up the contributions from both the TA and LA phonons. However, this approximation will become invalid in nanoscale devices. For example, the continuous miniaturization in device dimension and induction of nonuniform strain in the channel will significantly alter the electronic structures in the metal-oxide-semiconductor field-effect transistor (MOSFET) [17] and modify the relative importance of carrier scattering channels. Therefore, having precise deformation potentials of each phonon mode is essential to accurately predict the transport properties for advanced nanoscale devices toward developing predictive technology computer-aided design (TCAD). Although the first-principles method of carrier mobility can correctly capture the contributions from different phonon modes, the high computational cost of first-principles calculations prevents it from directly predicting carrier scattering or transport properties in nanoscale devices. This limitation poses a challenge to correctly assess the role of different phonon modes in device modeling. Fortunately, the recently developed first-principles methods [18–25] for carrier mobility have provided insights into the relative significance of all types of phonon-limited scatterings and accurately deduced deformation potentials, offering the possibility to predict instead of fitting the mobility in nanoscale devices. Specifically, Restrepo *et al.* [26] conducted a work on the first-principles calculations of the carrier mobilities in Si, followed by Li [20], Ma *et al.* [25], Giustino [18], Poncé *et al.* [19], Brunin *et al.* [24], and Zhou *et al.* [23]. In this paper, we revisit the carrier-phonon scattering mechanisms in Si based on first-principles calculations without *ad hoc* assumptions as made in classical scattering models. We show that our computed mobilities are in approximately good agreement with experiments over a wider temperature range from 100 to 600 K for both types of carriers. By the decomposition of the first-principles calculation-predicted e-ph scattering into the contributions from different phonon modes and electronic valleys, we show that TA scattering has an even comparable contribution with the LA scattering on carrier mobilities in Si, in striking contrast with the common belief that the TA mode is negligible. We reveal that it is primarily because the shear deformation potential associated with the TA mode was substantially underestimated previously and should be, in fact, much higher than the dilation deformation potential associated with the LA mode. Furthermore, we illustrate that TA phonons can lead to significant intraband scattering of carriers in anisotropic bands. We also discuss the effects of phonon-dependent conduction and valence band deformation potentials extracted from first-principles e-ph coupling matrix elements. These findings shed light on the role of TA phonons in carrier transport in semiconductors and could have important implications for the design of high-performance electronic devices.

This paper is organized as follows: In Sec. II, we present the formalism concerning the phonon-limited scattering rate as well as carrier mobilities, along with associated computational details. Section III A compares our theoretical carrier mobilities with experimental data. In Sec. III B 1 (and III C 1), we examine the role of decomposed phonon-limited scattering on electrons (holes), in contrast with alternative perspectives

found in the literature. Section III B 2 (and III C 2) discusses the types of phonons capable of participating in scattering via the selection rules based on the lowest-order e-ph interaction Hamiltonian. Section III B 3 (and III C 3) involves a comprehensive analysis of e-ph scattering matrix elements on electrons (and holes). Moreover, in Sec. III B 4 (and III C 4), we provide a demonstration of extracting deformation potentials from e-ph scattering matrix elements predicted by the first-principles method. Finally, our conclusions are drawn in Sec. IV.

II. COMPUTATIONAL METHODS

Under a low electric field, carriers gain energy from the electric field \mathbf{E} over the mean free path being much less than the thermal energy $k_B T$; subsequently, the phonon-limited relaxation time τ_{nk} for carriers located at the band n with a wave vector \mathbf{k} could associate directly with the imaginary part of the Fan-Migdal electron self-energy $\text{Im}\Sigma_{nk}^{\text{FM}}$ [19] as follows:

$$\begin{aligned} \frac{1}{\tau_{nk}} &= 2\text{Im}\Sigma_{nk}^{\text{FM}} = \sum_{m,\nu} \frac{1}{\tau_{nm,\mathbf{k}}^\nu} \\ &= \frac{2\pi}{\hbar} \sum_{m\nu} \int \frac{d\mathbf{q}}{\Omega_{\text{BZ}}} |g_{m\nu}(\mathbf{k}, \mathbf{k} + \mathbf{q})|^2 \\ &\quad \times \left[(1 - f_{m,\mathbf{k}+\mathbf{q}}^0 + n_{\nu,\mathbf{q}}) \delta(\varepsilon_{n,\mathbf{k}} - \varepsilon_{m,\mathbf{k}+\mathbf{q}} - \hbar\omega_{\nu,\mathbf{q}}) \right. \\ &\quad \left. + (f_{m,\mathbf{k}+\mathbf{q}}^0 + n_{\nu,\mathbf{q}}) \delta(\varepsilon_{n,\mathbf{k}} - \varepsilon_{m,\mathbf{k}+\mathbf{q}} + \hbar\omega_{\nu,\mathbf{q}}) \right]. \end{aligned} \quad (1)$$

Here, $1/\tau_{nm,\mathbf{k}}^\nu$ and $|g_{m\nu}(\mathbf{k}, \mathbf{k} + \mathbf{q})|$ are the e-ph scattering rate and corresponding scattering matrix element for an electron from the initial electronic state $|n, \mathbf{k}\rangle$ (with an eigenenergy $\varepsilon_{n,\mathbf{k}}$) into the final state $|m, \mathbf{k} + \mathbf{q}\rangle$ (with an eigenenergy $\varepsilon_{m,\mathbf{k}+\mathbf{q}}$) caused by a phonon $|\nu, \mathbf{q}\rangle$ (with a frequency $\omega_{\nu,\mathbf{q}}$). Here, $f_{m,\mathbf{k}}^0$ is the occupation number of the electronic state $|m, \mathbf{k}\rangle$ in the absence of the electric field according to the Fermi-Dirac distribution, $n_{\nu,\mathbf{q}}$ the occupation number of the phonon $|\nu, \mathbf{q}\rangle$ with branch index ν and wave vector \mathbf{q} according to the Bose-Einstein distribution function, and Ω_{BZ} is the volume of the BZ. To obtain a continuous density of states (DOS) for numerical stability, the sharp δ function is usually broadened by utilizing a broadening parameter η through a Lorentzian function.

Until recently, the e-ph scattering matrix element could be obtained from first-principles calculations utilizing density functional perturbation theory (DFPT) [28]:

$$g_{m\nu}(\mathbf{k}, \mathbf{k} + \mathbf{q}) = \sqrt{\frac{\hbar}{2M_0\omega_{\nu,\mathbf{q}}}} \langle u_{m,\mathbf{k}+\mathbf{q}} | \delta_{\nu,\mathbf{q}} V(\mathbf{r}) | u_{n,\mathbf{k}} \rangle, \quad (2)$$

where the perturbation potential $\delta_{\nu,\mathbf{q}} V(\mathbf{r})$ is obtained from the derivative of the self-consistent potential $V(\mathbf{r})$ with respect to a collective ionic displacement induced by the phonon $|\nu, \mathbf{q}\rangle$, $|u_{n,\mathbf{k}}\rangle$ and $|u_{m,\mathbf{k}+\mathbf{q}}\rangle$ are Bloch eigenstates of the initial electronic state $|n, \mathbf{k}\rangle$ and final state $|m, \mathbf{k} + \mathbf{q}\rangle$, respectively, and M_0 is the total mass of the unit cell. Once we learn the e-ph scattering rate τ_{nk} , we can calculate the carrier mobility tensor

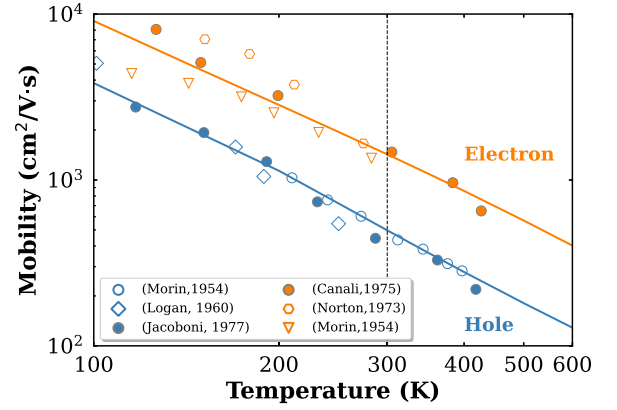


FIG. 1. Phonon-limited electron and hole mobilities as a function of temperature predicted using the first-principles Boltzmann formalism compared with experimental data. The discrete points represent experimental values adopted from the publications cited in Refs. [31–35]. The solid lines are computed by the first-principles method as implemented in the EPW package [28].

$\mu_{e,\alpha\beta}$ based on the self-energy relaxation time approximation:

$$\mu_{e,\alpha\beta} = -\frac{e}{\Omega n_e} \sum_n \int \frac{d\mathbf{k}}{\Omega_{\text{BZ}}} \cdot v_{nk}^\alpha v_{nk}^\beta \cdot \tau_{nk} \cdot \frac{\partial f_{nk}^0}{\partial \varepsilon_{nk}}, \quad (3)$$

where n_e is carrier density, Ω is the unit cell volume, and v_{nk}^α is group velocity along the α direction obtained from the derivative of the band dispersion through $\partial \varepsilon_{nk} / \partial \mathbf{k}_\alpha$.

First-principles calculations of the electronic band structure and phonon dispersion of bulk Si are performed by utilizing density functional theory (DFT) and DFPT, respectively, using a fully relativistic norm-conserving pseudopotential under the Perdew-Zunger exchange-correlation functional as implemented in the QUANTUM ESPRESSO package [27]. In DFT calculations, self-consistent and non-self-consistent field calculations use a uniform $12 \times 12 \times 12$ Γ -centered Monkhorst-Pack \mathbf{k} -point sampling of the BZ and an 80 Ry plane-wave energy cutoff, along with optimal lattice constant of 10.262 Bohr (or 5.43 Å) for Si. In the DFPT calculation, the dynamical matrices and the variation of perturbation potential induced by phonon modes are computed on a uniform $6 \times 6 \times 6$ \mathbf{q} -point grid. Once the electron and phonon eigenvalues ($\varepsilon_{m,\mathbf{k}}$ and $\omega_{\nu,\mathbf{q}}$) and perturbation potentials have been obtained from the DFT and DFPT calculations, the e-ph scattering matrix elements $g_{m\nu}$ and then carrier self-energy are ready to calculate. Finally, we compute the carrier mobilities based on the Boltzmann transport equation, as implemented in the EPW program [28], by interpolating the scattering matrix elements using Wannier functions for the interpolation of energy bands from a coarse BZ grid ($6 \times 6 \times 6$ \mathbf{q} -mesh and $12 \times 12 \times 12$ \mathbf{k} -mesh) to a dense grid with 85 000 \mathbf{k} points and 200 000 \mathbf{q} points [29,30].

III. RESULTS AND DISCUSSIONS

A. First-principles calculation-predicted phonon-limited electron and hole mobilities in Si

Figure 1 shows the first-principles predictions of phonon-limited (intrinsic) electron and hole mobilities in Si as a

function of temperature (ranging from 100 to 600 K) compared with experimental data [31–35]. Without accounting for defect-assisted and carrier-carrier scattering, theoretically predicted carrier mobilities align well with experimentally reported values across a wide temperature range but exhibit slight overestimation at lower temperatures, which indicates the contributions of defect-assisted and carrier-carrier scattering. Specifically, our first-principles calculations predict room-temperature mobilities for electrons and holes in silicon as $\mu_e \approx 1427 \text{ cm}^2/\text{Vs}$ and $\mu_h \approx 498 \text{ cm}^2/\text{Vs}$, respectively. These values fall within the ranges of experimentally measured drift mobilities of $\mu_e^{\text{expt}} = 1350\text{--}1500 \text{ cm}^2/\text{Vs}$ [19,31] and $\mu_h^{\text{expt}} = 450\text{--}505 \text{ cm}^2/\text{Vs}$ [19,31,36–38].

Such good agreement is achieved by employing a larger broadening parameter $\eta = 50 \text{ meV}$ instead of the more commonly utilized $\eta = 5 \text{ meV}$ [19]. According to Eqs. (1) and (3), carrier mobility depends not only on the e-ph scattering matrix elements but also on the band structure, which in turn relies on various computational parameters, including pseudopotentials, spin-orbit coupling, lattice parameters, and BZ sampling. Discrepancies in the treatment of these computational parameters lead to varying first-principles values of room-temperature electron mobility in Si as previously documented: $\mu_e = 1915 \text{ cm}^2/\text{Vs}$ [25], $1970 \text{ cm}^2/\text{Vs}$ [26], $1860 \text{ cm}^2/\text{Vs}$ [20], and $1305\text{--}1555 \text{ cm}^2/\text{Vs}$ [19]. Similarly, previously reported first-principles values of room-temperature hole mobility in Si are $\mu_h = 569 \text{ cm}^2/\text{Vs}$ [25] and $502\text{--}820 \text{ cm}^2/\text{Vs}$ [19]. The overestimation of these predicted mobilities primarily arises from the well-known deficiency of DFT in underestimating effective masses, defined by the second derivative of the band dispersion with respect to the wave vector in close proximity to the zone center for the hole. Poncé *et al.* [19] demonstrated that the GW correction to the DFT band structure could decrease the hole mobility by 2.8%, a finding consistent with our calculations. Our calculations indicate that the GW correction decreases room-temperature hole mobility from 510 to $498 \text{ cm}^2/\text{Vs}$, a value falling within the experimental range of $\mu_h^{\text{expt}} = 450\text{--}505 \text{ cm}^2/\text{Vs}$ [19,31,36–38]. On the other hand, two independent groups of Brunin *et al.* [24,39] and Jhalani *et al.* [40] and Park *et al.* [41] have recently demonstrated the impact of quadrupoles on carrier mobility, with Brunin *et al.* [39] revealing that quadrupoles can modify room-temperature mobility of Si by 9%. In this paper, we find that a larger broadening parameter η could also address these issues, as we can observe a reduction in hole mobility from 607 through 601 to $498 \text{ cm}^2/\text{Vs}$ by incrementally increasing η from 5 through 10 to 50 meV while utilizing the same DFT pseudopotentials as those adopted by Poncé *et al.* [19]. These agreements underscore the capability of the first-principles approach to properly predict carrier mobility without *ad hoc* assumptions, which are frequently involved in classical phenomenological models. It enables us to comprehensively capture all carrier-phonon scattering channels and revisit the underlying scattering mechanisms. It is noteworthy that the adjustable broadening parameter does not alter the results of the contribution of phonon-decomposed scattering rates and scattering matrix elements since it affects the mobility only through the energy conservation law as given in Eq. (1). The focus of this paper is on examining the scattering channels

instead of developing a method to predict carrier mobility more accurately.

B. Phonon-limited scattering for electrons in Si

1. Intravalley and intervalley scattering rates for electrons

We calculate the total carrier-phonon scattering rate by summing all components according to Eq. (1). Figure 2(a) shows the total scattering rate of an electron against the electron energy at a temperature of 300 K. Each point indicates a rate for an electron located at state $|n, \mathbf{k}\rangle$ with energy $\varepsilon_{n\mathbf{k}}$. In indirect band-gap Si, the conduction band minimum (CBM) is located at the Δ point, which has six equivalent points in the BZ, and thus, there are six Δ valleys. The long-wavelength phonons can only scatter electrons within a single valley (termed intravalley scattering), ensured by the momentum conservation law. In addition to intravalley scattering, the scattering of electrons from one Δ valley to another one (termed intervalley scattering) is also possibly caused by short-wavelength phonons, which are mainly located at the BZ edge. Therefore, we can further decompose the total scattering into intravalley and intervalley scatterings. Furthermore, if the intervalley scattering occurs between two Δ valleys chosen along two different (orthogonal) axes, it is named *f*-type intervalley scattering. Another type of intervalley scattering is between two Δ valleys chosen along the same axis and is named *g*-type intervalley scattering. One can learn from Fig. 2(a) that the long-wavelength limit intravalley scattering is the leading channel in the low-energy region (or near the CBM) as a result of the energy conservation and momentum conservation law. As electron energy increases, the *f*- and *g*-type intervalley scatterings grow up rapidly, which is absent in the intravalley scattering. The *f*-type intervalley scattering becomes the main scattering channel as the electron energy exceeds 0.15 eV.

To quantify the contribution of each scattering channel to the total scattering rate, we average the scattering rates $1/\tau_{n\mathbf{k}}^{\text{tot}}(i)$ (here, *i* stands for intravalley, *f*- and *g*-type intervalley, and the superscript tot for summing over all phonons) over energy bands with a finite occupation number and the whole BZ as follows:

$$\left\langle \frac{1}{\tau^{\text{tot}}(i)} \right\rangle = \frac{\sum_n \int_{\text{BZ}} \frac{1}{\tau_{n\mathbf{k}}^{\text{tot}}(i)} \cdot \frac{\partial f_{n\mathbf{k}}(\varepsilon_{n\mathbf{k}})}{\partial \varepsilon_{n\mathbf{k}}} d\mathbf{k}}{\sum_n \int_{\text{BZ}} \frac{\partial f_{n\mathbf{k}}(\varepsilon_{n\mathbf{k}})}{\partial \varepsilon_{n\mathbf{k}}} d\mathbf{k}}. \quad (4)$$

Figure 2(e) shows the contribution percentage of each scattering channel to the total e-ph scattering rate. We found that the intravalley scattering is the leading scattering channel with a contribution of 63.8%, followed by *f*-type intervalley scattering (28.3%). The *g*-type intervalley scattering only contributes 7.9%. These results contrast sharply with the most frequently quoted results in the textbooks. For instance, Yu and Cardona [3] in their classical textbook argued that the intervalley scattering processes are more significant than the intravalley scattering processes for the e-ph scattering in Si and Ge. Hamaguchi [6] suggested that the theoretical electron mobility can match well with the experimental data only when the strength of *g*-type intervalley scattering is comparable with that of the intravalley scattering. He considered the role of *f*-type intervalley scattering negligible since its associated

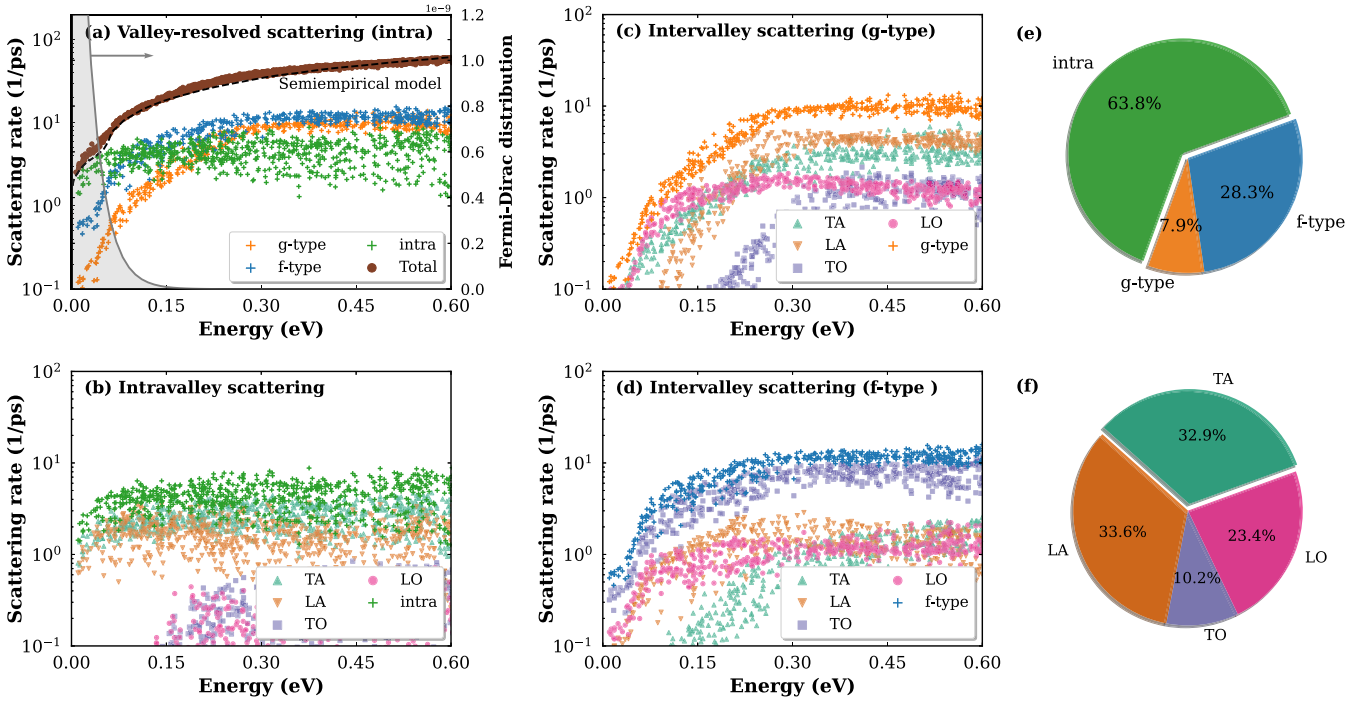


FIG. 2. (a) Intravalley (green dots) and intervalley (blue and orange dots for f and g types, respectively) scattering and total scattering rates (black dots) for electrons in Si at 300 K. The dashed red line represents the total scattering rate based on the semiempirical model including acoustic-deformation-potential and intervalley optical-deformation-potential scattering, which has been shown in earlier work [8]. (b)–(d) Decomposed phonon-limited intravalley, g -type, and f -type scattering into TA, LA, LO, and TO modes, respectively. (e) Pie chart representation of the percentages of intravalley scattering (green region), g -type intervalley scattering (orange region), and f -type intervalley (blue region) electron-phonon (e-ph) scattering at room temperature. (f) The contributions of TA, LA, LO, and TO modes to the total e-ph scattering rate. Note that TA is a sum of two transverse acoustic modes (TA1 and TA2); LA represents the longitudinal acoustic mode; TO is a sum of two transverse optical modes (TO1 and TO2); and LO represents the longitudinal optical mode.

deformation potentials are much smaller than that of the g -type process.

We can further decompose the intravalley, f -type intervalley, and g -type intervalley scatterings into phonons of TA, LA, TO, and LO modes, as illustrated in Figs. 2(b)–2(d). Similarly, to quantify the contribution of different phonon modes to the total scattering rate, we average the scattering rates $\frac{1}{\tau^\nu(i)}$ (here, ν denotes the phonon mode, such as TA, LA, TO, and LO) over the whole BZ as follows:

$$\left\langle \frac{1}{\tau^\nu(i)} \right\rangle = \frac{\sum_n \int_{\text{BZ}} \frac{1}{\tau_{nk}^\nu(i)} \cdot \frac{\partial f_{nk}(\epsilon_{nk})}{\partial \epsilon_{nk}} d\mathbf{k}}{\sum_n \int_{\text{BZ}} \frac{\partial f_{nk}(\epsilon_{nk})}{\partial \epsilon_{nk}} d\mathbf{k}}. \quad (5)$$

Here, phonon modes ν are approximately distinguished through projecting the phonon eigenmode near the BZ center $\mathbf{q}_\Gamma = (0, 0, 0)$ for the intravalley scattering, \mathbf{q}_f [e.g., $(0.82, 0.82, 0)2\pi/a$] for f -type intervalley scattering, and \mathbf{q}_g [e.g., $(1.64, 0, 0)2\pi/a$] for g -type intervalley scattering based on the momentum conservation law.

Figure 2(f) shows the contribution of each phonon mode ν to the total scattering rate $\sim \langle 1/\tau^\nu \rangle / \sum_\nu \langle 1/\tau^\nu \rangle$. Surprisingly, scattering from the TA mode is unexpectedly strong [3], which is even comparable with the contribution from the LA mode to total e-ph scattering and contrary to the common perception that the TA mode is negligible in e-ph scattering for electrons in Si [6,8,42]. Specifically, the intravalley scattering is predominantly caused by AC phonons

[$\sim 99\%$ contribution according to Eq. (5)] with a negligible contribution from OP phonons, as shown in Fig. 2(b). This result aligns with the selection rules based on symmetry analysis [3], which identifies that the OP phonons are forbidden in the intravalley scattering. However, one can also see that the TA mode possesses a comparable contribution with the LA mode to the intravalley scattering, as shown in Fig. 2(b), and is indeed negligible in both f - and g -type intervalley scatterings, as shown in Figs. 2(c) and 2(d). Therefore, the TA mode phonons presented in the e-ph scattering are exclusively involved in intravalley scattering. In f -type intervalley scattering, Fig. 2(d) shows that the TO mode provides the predominant scattering channel [58% contribution according to Eq. (5)] with finite contributions from LA and LO phonons. This result is different from previous reports, which underscored the larger contributions of the LO and LA modes than the TO mode in f -type intervalley scattering [6] despite the selection rule allowing only the LA- and TO-assisted transitions in f -type intervalley scattering [3]. For g -type intervalley scattering, however, the TO mode is negligible since the LO mode primarily governs the scattering at low-energy regions and the LA mode dominates the scattering at high-energy regions, as shown in Fig. 2(c). Note that the LA mode is less important to total scattering due to its modest contribution [constituting only 8% according to Eq. (5)] as a result of its small occupation number. This finding disputes the conclusion in the literature [3,12,43] that LA scattering is so strong that its in-

clusion in g -type intervalley scattering becomes necessary to explain the experimentally observed temperature dependence of the electron mobility in Si.

2. Symmetry analysis and selection rules based on the scattering matrix

Bir and Pikus [9] illustrated that the e-ph scattering transitions between two arbitrary \mathbf{k} points \mathbf{k}_i and \mathbf{k}_f [which is equal to $\mathbf{k}_i + \mathbf{q}$ in Eq. (1)] are subject to the selection rules of their nearby extrema \mathbf{k}_{0i} and \mathbf{k}_{0f} of sufficiently high symmetry regarding the probability of transitions from \mathbf{k}_i to \mathbf{k}_f will be small if the transitions from \mathbf{k}_{0i} to \mathbf{k}_{0f} are forbidden by symmetry. Selection rules must, therefore, be determined specifically for band extremum points, which are Γ , X , and L points in conventional semiconductors. Here, we revisit the selection rules according to the classical phenomenological models. According to Eq. (1), it is straightforward to learn that the key factor governing e-ph scattering is the e-ph scattering matrix element, which describes the strength of an electron being scattered from the initial electronic state $\psi_{n\mathbf{k}}$ to the final electronic state $\psi_{m\mathbf{k}+\mathbf{q}}$ by a phonon with mode μ and wave vector \mathbf{q} :

$$g_{nmv}^{\text{tot}} = \langle \psi_{m\mathbf{k}+\mathbf{q}} | H_{\text{e-ph}}(v) | \psi_{n\mathbf{k}} \rangle. \quad (6)$$

The scattering matrix element g_{nmv} provides a selection rule depending on the symmetries of the e-ph Hamiltonian and initial and final electron states. Thus, which phonon modes interact with the electrons depends upon the symmetries of the initial and final electronic states and whether an Umklapp process is involved (as is the case for intervalley scattering). To gain insight into the e-ph interaction and to link with classical e-ph scattering models, the scattering rate for each phonon mode must be considered separately. To do so, we could construct the e-ph interaction Hamiltonian $H_{\text{e-ph}}$ utilizing the phenomenologically effective e-ph interaction Hamiltonian. In Si, a nonpolar semiconductor in which the Fröhlich and piezoelectric e-ph interactions are absent, $H_{\text{e-ph}}$ can be decomposed into H_{ADP} causing ADP scattering, H_{ODP} causing ODP scattering for intravalley scattering, and H_{IV} for intervalley scattering, given by

$$H_{\text{e-ph}} = H_{\text{ADP}} + H_{\text{ODP}} + H_{\text{IV}}. \quad (7)$$

a. Selection rules for phonon-limited scattering of Γ -valley electrons. The energy and momentum conservation laws restrict e-ph intravalley scattering to AC or OP phonon modes with small \mathbf{q} (named the long-wavelength limit). The atomic displacement caused by the long-wavelength AC phonons is like that caused by a macroscopic strain of the crystal, of which the effect on energy can be described by deformation potentials according to DPT [2]. Thus, analogous to the strain Hamiltonian, the electron-AC-phonon interaction Hamiltonian H_{ADP} can be defined as [4,9,42,44]

$$H_{\text{ADP}} = \sum_{\alpha,\beta} \Xi_{\alpha\beta}^{n\mathbf{k}} \cdot \epsilon_{\alpha\beta}. \quad (8)$$

Here, $\Xi_{\alpha\beta}^{n\mathbf{k}}$ are deformation potentials for an electron state in an energy band n and wave vector \mathbf{k} , and $\epsilon_{\alpha\beta} = \frac{1}{2} \left(\frac{\partial \delta \mathbf{R}_\alpha}{\partial \mathbf{R}_\beta} + \frac{\partial \delta \mathbf{R}_\beta}{\partial \mathbf{R}_\alpha} \right)$ is a strain tensor describing the homogeneous defor-

TABLE I. Part of compatibility relations between the Γ point in the O_h group and the symmetry axis (Δ , Σ , and Λ) in the diamond structure. The notation is that of Koster (molecular) notation [48,49].

Γ point (O_h)	Δ axis (C_{4v})	Σ axis (C_{2v})	Λ axis (C_{3v})	L point (D_{3d})
Γ_1 (A_{1g})	Δ_1 (A_1)	Σ_1 (A_1)	Λ_1 (A_1)	L_1 (A_{1g})
Γ_4^- (T_{1u})	$\Delta_1 \oplus \Delta_5$ ($A_1 \oplus E$)	$\Sigma_1 \oplus \Sigma_3 \oplus \Sigma_4$ ($A_1 \oplus B_2 \oplus B_1$)	$\Lambda_1 \oplus \Lambda_3$ ($A_1 \oplus E$)	$L_2' \oplus L_3'$ ($A_{2u} \oplus E_u$)
Γ_5^+ (T_{2g})	$\Delta_4 \oplus \Delta_5$ ($B_2 \oplus E$)	$\Sigma_1 \oplus \Sigma_2 \oplus \Sigma_3$ ($A_1 \oplus A_2 \oplus B_2$)	$\Lambda_1 \oplus \Lambda_3$ ($A_1 \oplus E$)	$L_1 \oplus L_3$ ($A_{1g} \oplus E_g$)

mation of a crystal induced by long-wavelength AC phonons (here, $\delta \mathbf{R}$ represents the AC-phonon-induced displacement, of which that located at BZ center belongs to the T_{1u} representation in the O_h point group). Note that, the representation T_{1u} is expressed in Molecular notation, also named as the Γ_4^- representation in Koster notation. Commonly, the Koster notation could be linked to the Molecular notation according to Table I. Since both $\Xi_{\alpha\beta}^{n\mathbf{k}}$ and $\epsilon_{\alpha\beta}$ are symmetrical second-rank tensors, nine elements reduce to six independent quantities. In general, six deformation potentials are required to describe the strain Hamiltonian without considering the symmetry of wave vector \mathbf{k} , which could further reduce the number of independent elements. Notably, the symmetry of the strain Hamiltonian H_{ADP} is determined by the direct product of the symmetry of the vector \mathbf{R} with the symmetry of the AC phonon displacement $\delta \mathbf{R}$ under the wave vector group for a particular \mathbf{k} point since deformation potential constants $\Xi_{\alpha\beta}^{n\mathbf{k}}$ are scalar. Note that the AC phonons at the Γ point belong to T_2 in the zinc-blende structure (T_d point group) and belong to T_{1u} in diamond structure (O_h point group). Considering the symmetry, the strain Hamiltonian H_{ADP} for electrons located at the CBM in Si can be described by two independent deformation potential constants Ξ_d and Ξ_u , through the relationship $\Xi_d = \Xi_{xx} = \Xi_{yy}$ and $\Xi_u = \Xi_{yy} - \Xi_{zz}$.

Unlike AC phonons, long-wavelength OP phonons possess finite energy, and thus, the atomic displacement induced by the long-wavelength OP phonons can affect the electronic energy of the involved electron states directly. Subsequently, the electron-OP-phonon interaction is a zeroth-order Hamiltonian with the form [3,6,8]:

$$H_{\text{ODP}} = \Xi_{\text{ODP}}^{n,\mathbf{k}} \cdot \delta \mathbf{R}. \quad (9)$$

Here, $\delta \mathbf{R}$ represents the relative displacement of two atoms in the unit cell caused by long-wavelength OP phonons. The symmetry of H_{ODP} is simply determined by the symmetry of OP-phonon-induced displacement $\delta \mathbf{R}$. Note the OP phonons located at the BZ center belong to T_2 representation in the T_d point group or T_{2g} representation in the O_h point group.

Most semiconductors have direct band gaps with both CBM and valence band maximum (VBM) located at the Γ point [3]; the scattering of electrons in the nondegenerate s -like Γ valley is well established based on a simple single isotropic band. Specifically, in zinc-blende GaAs (diamond Si) crystal, the wave vector group of the Γ point is the T_d point group in zinc-blende structure (or the O_h point group in diamond structure), in which both the vector \mathbf{R} of atomic

TABLE II. Summary of the selection rules of carrier scattering from the initial state $|i\rangle$ with irreducible representation G_i to the final state $|f\rangle$ with representation G_f by phonons with TA, LA, TO, and LO modes, respectively [45–47]. The numbers in parentheses beneath the states are k wave vectors. Production stands for symmetry production of the initial and final states under the group of wave vector with the symbol in parentheses.

Initial state $ i\rangle, G_i$	Final state $ f\rangle, G_f$	Production $G_i \otimes G_f$	e-ph Hamiltonian H_{e-ph}			$\langle f H_{e-ph} i\rangle$
			$(H_{ADP}, H_{ODP}, H_{IV})$			
$A_{1g}(\Gamma_{1c})$ (0,0,0)	$A_{1g}(\Gamma_{1c})$ (0,0,0)	A_{1g} (O_h)	H_{ADP} :	LA	$A_{1g} \oplus E_g \oplus T_{2g}$	$\neq 0$
			$(A_{1g} \oplus E_g \oplus T_{2g})$	TA	$E_g \oplus T_{2g}$	0
			H_{ODP} :	LO	T_{2g}	0
			(T_{2g})	TO	T_{2g}	0
$T_{2g}(\Gamma_5^+)$ (0,0,0)	$T_{2g}(\Gamma_5^+)$ (0,0,0)	$A_{1g} \oplus E_g \oplus T_{2g} \oplus T_{1g}$ (O_h)	H_{ADP} :	LA	$A_{1g} \oplus E_g \oplus T_{2g}$	$\neq 0$
			$(A_{1g} \oplus E_g \oplus T_{2g})$	TA	$E_g \oplus T_{2g}$	$\neq 0$
			H_{ODP} :	LO	T_{2g}	$\neq 0$
			(T_{2g})	TO	T_{2g}	$\neq 0$
$A_1(\Delta_{1c})$ (u,0,0)	$A_1(\Delta_{1c})$ (u,0,0)	A_1 (C_{4v})	H_{ADP} :	LA	$A_1 \oplus E$	$\neq 0$
			$(A_1 \oplus E \oplus B_1 \oplus B_2)$	TA	$A_1 \oplus E \oplus B_1 \oplus B_2$	$\neq 0$
			H_{ODP} :	LO	B_2	0
	$A_1(\Delta_{1c})$ (-u,0,0)	B_2 (C_{4v}) (g type)	$H'_{IV}(AC)$:	LA	A_1	0
			$(A_1 \oplus E)$	TA	E	0
			$H'_{IV}(OP)$:	LO	B_2	$\neq 0$
			$(B_2 \oplus E)$	TO	E	0
	$A_1(\Delta_{1c})$ (0, \pm u,0) (f type)	$A_1 \oplus B_1$ (C_{2v})	$H'_{IV}(AC)$:	LA	A_1	$\neq 0$
			$(A_1 \oplus B_1 \oplus B_2)$	TA	$B_2 \oplus B_1$	0 ^a
			$H'_{IV}(OP)$:	LO	B_2	0
$(B_2 \oplus A_1 \oplus A_2)$	TO	$A_1 \oplus A_2$	$\neq 0$			

^aForbidden due to time-reversal symmetry.

positions and AC-phonon-induced displacement $\delta\mathbf{R}$ belong to the T_2 irreducible representation (or the T_{1u} irreducible representation of the O_h point group).

The strain tensor is related to both \mathbf{R} and $\delta\mathbf{R}$, and its symmetry should be a direct product of the symmetry of \mathbf{R} and $\delta\mathbf{R}$: $T_2 \otimes T_2 = A_1 \oplus E \oplus T_2 \oplus T_1$ in GaAs (or $T_{1u} \otimes T_{1u} = A_{1g} \oplus E_g \oplus T_{2g} \oplus T_{1g}$ in diamond Si). However, the strain tensor is symmetric and is incompatible with the antisymmetric T_1 (or T_{1g}) representation. Thus, the AC-phonon strain Hamiltonian H_{ADP} has a symmetry of $A_1 \oplus E \oplus T_2$ (or $A_{1g} \oplus E_g \oplus T_{2g}$ in diamond Si), as given in Table II. The LA mode component of the strain Hamiltonian belongs to A_1 (or A_{1g} in diamond Si), indicating that the LA-phonon-induced displacement $\delta\mathbf{R}$ produces a volume dilation strain associated with A_1 (A_{1g}) symmetry, while the shear TA mode component belongs to $E \oplus T_2$ ($E_g \oplus T_{2g}$), indicating that the TA-phonon-induced displacement produces a shear strain associated with E or T_2 (E_g or T_{2g}) symmetry. Subsequently, the scattering matrix element of electrons between two nondegenerate s -like Γ_1 electron states (A_1 representation in molecular notation) caused by LA phonons is nonzero since the direct product of the irreducible representations of the initial and final electron states (A_1 in the T_d point group or A_{1g} in the O_h point group) and strain Hamiltonian (A_1 in the T_d point group or A_{1g} in the O_h point group) involved in the scattering matrix element is $A_1 \otimes A_1 \otimes A_1 = A_1$ (or $A_{1g} \otimes A_{1g} \otimes A_{1g} = A_{1g}$ in the O_h group) and contains the scalar representation A_1 (A_{1g} as shown in Table II); whereas the TA-phonon-caused scattering matrix element of electrons between two A_1 states is zero because the direct product $A_1 \otimes (E \oplus T_2) \otimes A_1$ [or $A_{1g} \otimes (E_g \oplus T_{2g}) \otimes$

A_{1g} in the O_h group] contains no A_1 (A_{1g} as shown in Table II). Moreover, the electron-OP-phonon strain Hamiltonian H_{ODP} has a symmetry T_2 (or T_{2g} in the O_h group), giving rise to scattering matrix element vanishing since $A_1 \otimes T_2 \otimes A_1 = T_2$ ($A_{1g} \otimes T_{1u} \otimes A_{1g} = T_{1u}$). Therefore, it is well known that LA phonons dominate e-ph scattering in the nondegenerate conduction band with negligible contribution from the TA and TO phonons [6,8,42].

To confirm it, we have taken GaAs, a prototypical direct-band-gap semiconductor, as an example to examine the first-principles results. Figure 3 illustrates the scattering matrix element $|g_{m\nu}(\mathbf{k}, \mathbf{k} + \mathbf{q})|$ related to both electrons of GaAs in the s -like Γ valley and AC phonons along different wave vector directions, where we have temporarily disregarded the long-range part of the matrix elements. The electron-TA-phonon scattering is much weaker than the electron-LA-phonon scattering, indicating that TA phonons have little effect on the scattering of electrons in the s -like Γ valley.

b. Selection rules for intravalley scattering of Δ -valley electrons. In indirect-band-gap Si, however, electron-AC-phonon scattering differs from direct-band-gap GaAs because its CBM is located at six equivalent Δ points (close to the X points) in the first BZ. Thus, AC phonons can scatter electrons from one state to another within the same valley (intravalley scattering) or from one valley to another (intervalley scattering). In intravalley scattering, both the initial and final electron states have nearly the same \mathbf{k} vector as the one of the Δ points, and thus, the scattering matrix is invariant under the transformations of the C_{4v} wave vector group of a Δ point.

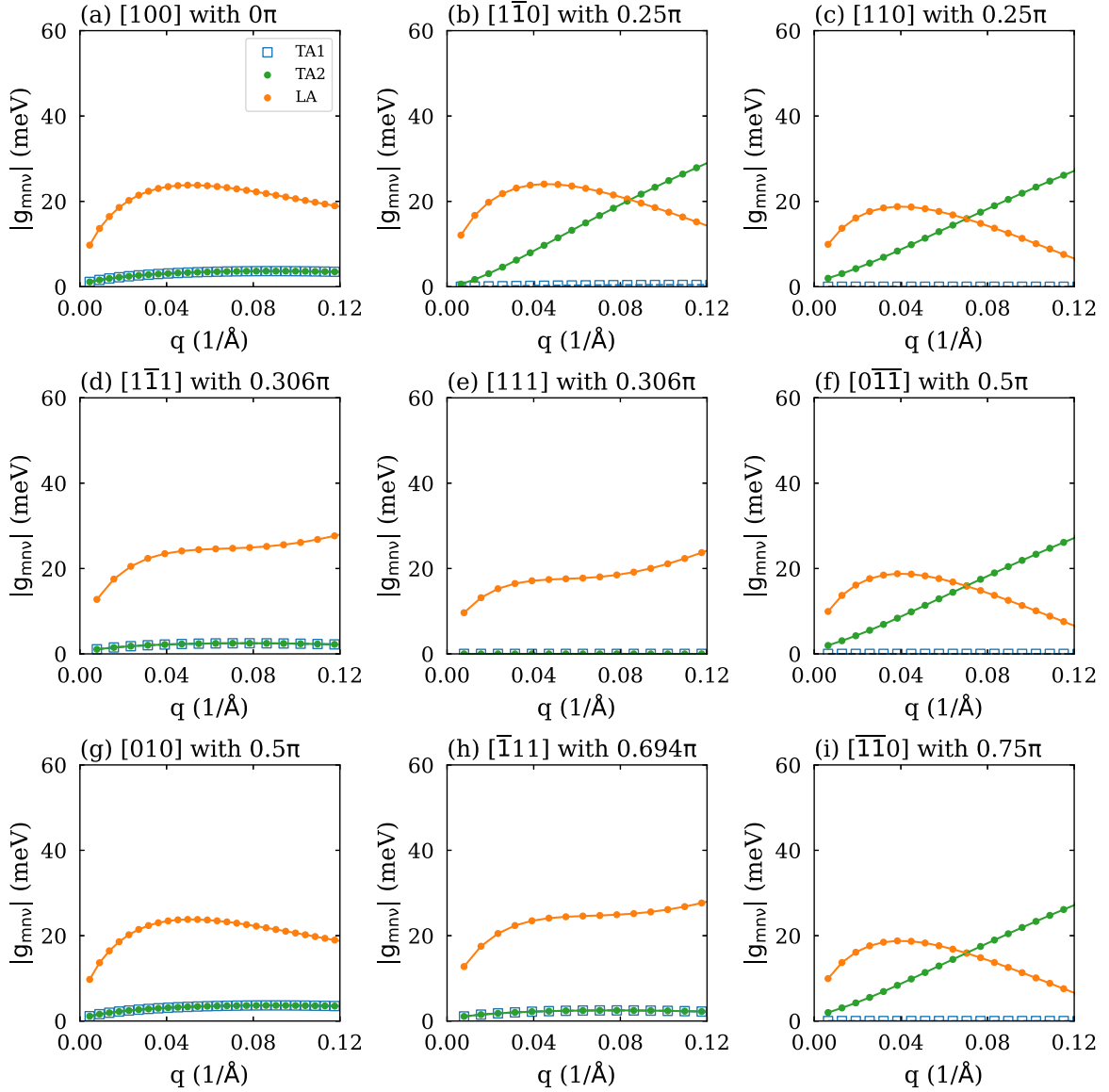


FIG. 3. (a)–(i) Intraband electron-phonon (e-ph) scattering matrix elements $g_{mnv}(\mathbf{k}, \mathbf{k} + \mathbf{q})$ for the conduction band of GaAs vs the phonon wave vector \mathbf{q} along several directions with $\theta = 0, 0.25, 0.306, 0.5, 0.694,$ and 0.75π . The initial electronic state $|n, \mathbf{k}\rangle$ is located at the conduction band minimum (CBM; Γ) for electrons, whereas the corresponding final states $|n, \mathbf{k} + \mathbf{q}\rangle$ are in the same band.

The electron state of the Δ valley belongs to the A_1 (Δ_1 in Koster notation) irreducible representation of the wave vector point group C_{4v} , and the direct product of the initial state with the final state is $A_1 \otimes A_1 = A_1$ (or $\Delta_1 \otimes \Delta_1 = \Delta_1$ in KSW notation). Under the C_{4v} wave vector group, the vector of atomic positions transforms as $A_1 \oplus E$, the LA phonon transforms as A_1 (Δ_1), and the TA phonon as E (Δ_5), as displayed in Fig. 4(b). Therefore, the AC-phonon strain Hamiltonian has a symmetry of $A_1 \oplus B_1 \oplus B_2 \oplus E$ since $(A_1 \oplus E) \otimes (A_1 \oplus E) = 2A_1 \oplus A_2 \oplus B_1 \oplus B_2 \oplus 2E$ and the antisymmetric A_2 is incompatible with the symmetric strain tensor in the Hamiltonian. The LA component of the strain Hamiltonian is associated with $A_1 \oplus E$ symmetry, and the TA component is associated with $A_1 \oplus B_1 \oplus B_2 \oplus E$ symmetry, as given in Table II. Since both the LA and TA strain Hamiltonians contain A_1 representation, the scattering matrix element is nonzero for both LA and TA phonons, scattering electrons within the

same valley in Si (given in Table I for intravalley scattering). Under the C_{4v} wave vector group, the electron-OP-phonon strain Hamiltonian H_{ODP} has a symmetry of $B_2 \oplus E$ because OP phonons belong to T_{2g} in the O_h point group and transform according to $B_2 \oplus E$ in the C_{4v} point group, and thus, the scattering matrix element between two A_1 electron states is zero. It indicates that OP phonons are forbidden for e-ph intravalley scattering.

c. Selection rules for intervalley scattering of Δ -valley electrons. In addition to intravalley scattering, intervalley scattering contributes significantly to e-ph scattering in indirect-band-gap semiconductors such as Si. The momentum conservation law demands short-wavelength (large-wave-vector) phonons involved in intervalley scattering since any two different Δ valleys in Si are separated by a \mathbf{k} vector with a finite length. These short-wavelength phonons at or near the zone edge have frequencies virtually independent

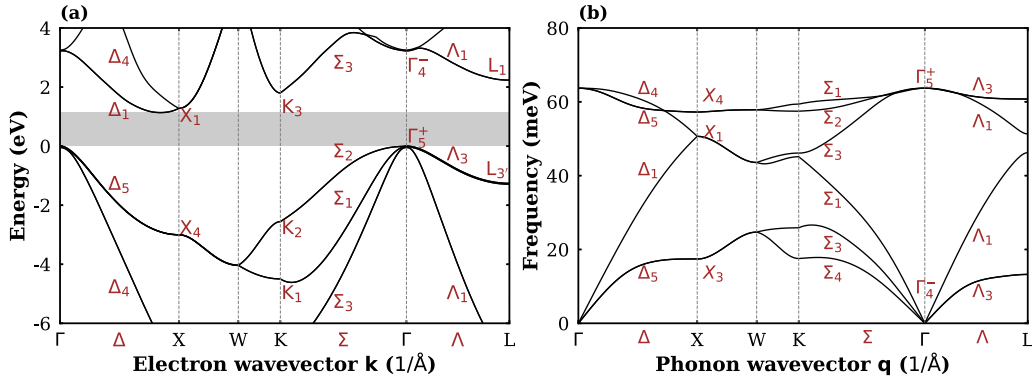


FIG. 4. (a) Electronic band structure of Si. The conduction band minima occur along the Γ -X at ~ 0.82 of the Brillouin zone (BZ) edge with Δ_1 representation. The valence band maximum is located at the center of the BZ with Γ_5^+ representation. (b) Phonon dispersion curves of Si. The lowest three branches are acoustic phonons and high-lying three branches are optical phonons, which are both threefold degenerate at Γ (acoustic phonons belong to Γ_4^- and optical phonons belong to Γ_5^+ of diamond structure O_h point group) and split into nondegenerate longitudinal acoustic (LA) and longitudinal optic (LO) and twofold degenerate transverse acoustic (TA) and transverse optic (TO), respectively, along the Γ -X direction (phonons along this direction are so-called Δ phonons). Along the $\langle 110 \rangle$ direction from Γ to K, the threefold degenerate acoustic (optical) phonons (called the Σ phonons) split into three modes belong to irreducible representations Σ_1 , Σ_3 , and Σ_4 (Σ_1 , Σ_2 , and Σ_3) of the wave vector group C_{2v} .

of the wave vector, whether OP or AC modes. The finite energy of these short-wavelength phonons renders their induced displacements to directly affect the electronic energy in scattering. Therefore, the intervalley e-ph interaction is a zeroth-order Hamiltonian like the electron-OP-phonon interaction Hamiltonian given in Eq. (9) and is defined as [3,8,50]

$$H_{IV} = \Xi_{ij} \cdot \delta \mathbf{R}. \quad (10)$$

Here, Ξ_{ij} is the intervalley deformation potential for an electron scattered from Δ valley i to Δ valley j ($i \neq j$), and the Hamiltonian H_{IV} has the symmetry of the phonon-induced displacement $\delta \mathbf{R}$. We should note that AC and OP phonons could be involved in intervalley scattering. Due to the wave vectors of the initial and final electron states being different in intervalley scattering, the transformations that leave the scattering matrix invariant are those common to both wave vectors [51]. The group formed from these common transformations is named the intersection group, which may be lowered from the C_{4v} wave vector group of the Δ point to the C_{2v} group, e.g., Σ phonons participate in f -type intervalley scattering. Another type of intervalley scattering is by Δ phonons, named g -type intervalley scattering, in which the intersection group remains the C_{4v} group.

For g -type intervalley scattering, electrons are scattered from a given Δ valley [say $\mathbf{k} = (u, 0, 0)$, $u = 0.82 \times \frac{2\pi}{a}$] to one on the opposite side ($-\mathbf{k}$) of the same axis, and the direct product of the initial Δ valley with the opposite Δ valley is $\Delta_1(\mathbf{k}) \otimes \Delta_1(-\mathbf{k}) = \Delta_1(2\mathbf{k})$ under the C_{4v} group. Because $|\mathbf{k}| = 0.82(2\pi/a)$ is larger than half the zone edge X and $2\mathbf{k}$ is a vector entering the second BZ, $\Delta_1(2\mathbf{k})$ needs to be translated back to the first zone by subtracting $4\pi/a$, giving rise to $\Delta_1(2\mathbf{k})$ transforming as Δ_4 (or B_2 in molecular notation) of the C_{4v} group [45]. Furthermore, Table II shows that the LA and TA phonons transform according to the A_1 and E irreducible presentations of the C_{4v} group, respectively. Therefore, both LA and TA phonon modes are absent in the g -type intervalley scattering, whereas the LO and TO phonons transform according to B_2 and E irreducible presentations of

the C_{4v} group, respectively, indicating that the LO phonons could participate in g -type intervalley scattering, but TO with E symmetry is absent.

For f -type intervalley scattering, electrons are scattered from say the $\mathbf{k} = (u, 0, 0)$ valley to the $\mathbf{k}' = (0, u, 0)$ valley by a Σ phonon with $\mathbf{q}' = (-u, u, 0)$; the selection rule between the initial and final electron states is $\Delta_1(\mathbf{k}) \otimes \Delta_1(\mathbf{k}') = \Sigma_1 \oplus \Sigma_4(\mathbf{q}')$ (or $A_1 \oplus B_1$ in molecular notation) [46]. In the C_{2v} intersection group of f -type intervalley scattering, the LA phonons transform as A_1 and TA phonons as $B_2 \oplus B_1$, giving rise to the LA component of H_{IV} associated with A_1 symmetry and TA component associated with $B_2 \oplus B_1$ symmetry. It indicates that both LA and TA modes can participate in f -type intervalley scattering according to the point-group theory of scattering matrix element. However, it was found that the latter is forbidden according to time-reversal symmetry [45–47], while the LO- and TO-phonon-induced displacements transform according to B_2 and $A_1 \oplus A_2$ irreducible presentations of the intersection group C_{2v} , respectively. Therefore, LO phonons are forbidden, and TO phonons are allowed in f -type intervalley scattering, as shown in Table II.

The selection rules in the above discussion are based on the lowest-order e-ph interaction Hamiltonian for each phonon mode. The long-wavelength AC phonons possess almost zero energy, and their atomic displacements cannot affect the electronic energies directly. Therefore, the zeroth-order term in atomic displacements is absent in the AC deformation Hamiltonian. However, the strain of the gradient of the atomic displacements in a crystal can shift the electronic energies. Therefore, the first-order term (strain) is the lowest order of the AC deformation Hamiltonian H_{ADP} . In contrast, the OP phonon deformation Hamiltonian and intervalley Hamiltonian consider only the zeroth-order term because associated phonons have finite energy, and the atomic displacements of these finite-energy phonons can affect the electronic energy directly. Therefore, in the presence of the zeroth-order term, the first-order term is usually disregarded due to its

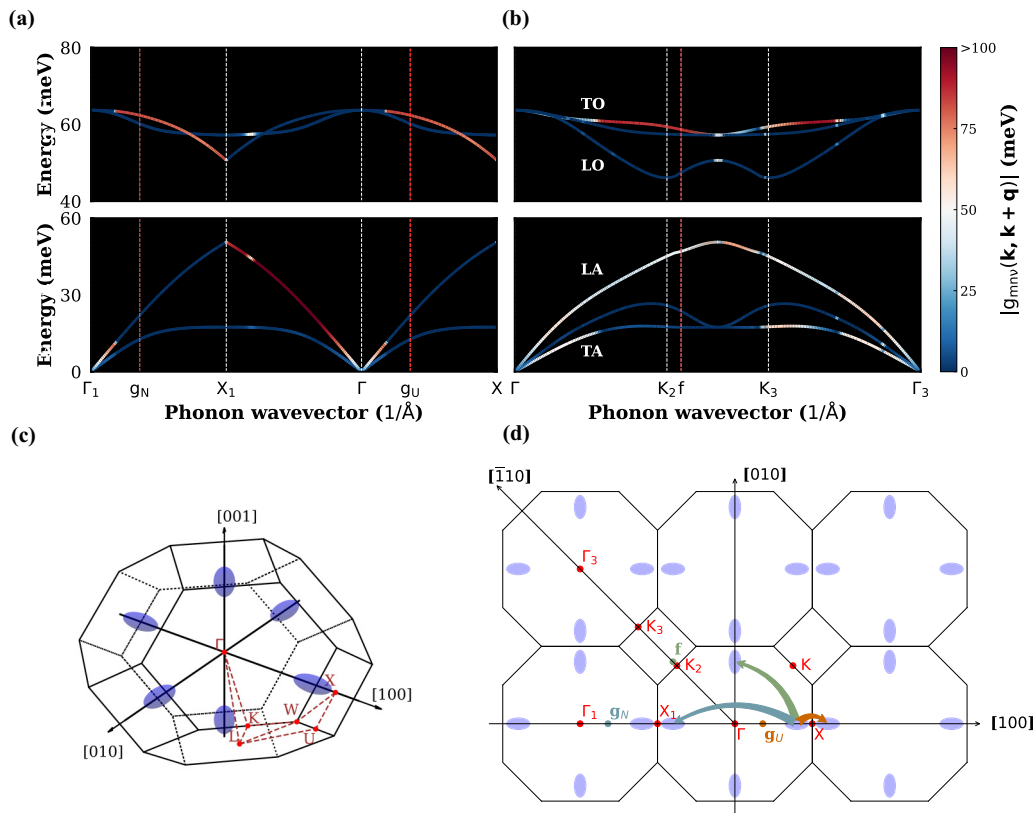


FIG. 5. The phonon structure of Si with a color map of the electron-phonon (e-ph) scattering matrix elements $|g_{mnv}(\mathbf{k}, \mathbf{k} + \mathbf{q})|$ at 300 K for band indexes m and n located at the lowest conduction band $\mathbf{k} = (0.82, 0, 0)(2\pi/a)$ and phonon wave vector \mathbf{q} along the high-symmetry path: (a) Γ_1 - X_1 - Γ - X along the [100] direction entering into the adjacent Brillouin zone (BZ; here, the high-symmetry path X_1 - Γ - X is in the first BZ, while X_1 - Γ_2 are inside the adjacent BZ), and (b) Γ - K_2 - K_3 - Γ_3 along the $[\bar{1}10]$ direction entering into the second and third BZ (here, Γ and K points are in the first BZ and Γ_3 and K_3 points are their counterparts in the other BZ). An electron with Δ_1 symmetry at $\mathbf{k} = (0.82, 0, 0)(2\pi/a)$ can be scattered into the opposite valley $\mathbf{k}' = (-0.82, 0, 0)(2\pi/a)$ along the same axis or equivalent nearby valley $\mathbf{k}' = (1.18, 0, 0)(2\pi/a)$ in the adjacent BZ via phonons with finite wave vector \mathbf{q} , labeled as g_N and g_U , respectively. The former and the latter represent normal and Umklapp g -type intervalley scattering, respectively. Similarly, an electron with Δ_1 symmetry at $\mathbf{k} = (0.82, 0, 0)(2\pi/a)$ can be scattered into the equivalent perpendicular valley $\mathbf{k}' = (0, 0.82, 0)(2\pi/a)$ in the same BZ along the Σ axis via Σ phonons with a wave vector labeled as f . (c) Schematic diagram of the first BZ in Si. (d) Schematic diagram of the g - and f -type intervalley scattering for electrons in the conduction band minimum (CBM) of Si, showing the involved phonon wave vectors.

relatively weak strength. We note that the LO-related f -type intervalley scattering process makes significant contributions based on first-principles calculations, although they are forbidden according to the selection rules given in Table II. It illustrates that the first-order term arising from strain (in analogy to the AC deformation Hamiltonian) must be considered once the zeroth order is forbidden by symmetry for a specific phonon mode. Specifically, the LO-phonon-induced first-order Hamiltonian $H_{IV}^{(1)}$ for f -type intervalley scattering can be described as the strain Hamiltonian, like Eq. (8). Thus, the symmetry of this first-order Hamiltonian is constructed by the direct product of the symmetries of a vector and of LO-phonon displacements, denoted as $A_1 \oplus A_2 \oplus B_2$ (or $\Sigma_1 \oplus \Sigma_2 \oplus \Sigma_3$), rendering the scattering matrix element of LO-related f -type intervalley scattering to be finite. It explains why first-principles calculation predicts finite LO-related f -type scattering, as shown in Fig. 2(d), although it is forbidden according to symmetry analysis as given in Table II.

3. First-principles calculations of scattering matrix elements for electrons in Si

While selection rules are applicable for determining whether the scattering transitions induced by a specific phonon mode are allowed or forbidden, assessing their relative strength presents a more intricate challenge. In this section, we will delve into the relative importance of e-ph scattering matrix elements concerning intravalley and intervalley scattering.

a. Intravalley scattering matrix elements. Figure 5 shows the intravalley scattering matrix elements $|g_{mnv}(\mathbf{k}, \mathbf{k} + \mathbf{q})|$ obtained via first-principles calculations for different phonon modes ν , plotted against the phonon wave vector \mathbf{q} at room temperature in Si. Specifically, we consider the scenario of an electron originating from one of the six equivalent Δ valleys, specifically at $\mathbf{k} = (0.82, 0, 0)(2\pi/a)$. Along the Γ - X direction, one can see from Fig. 5(a) that LA phonons possess the largest scattering matrix element among all phonon modes including TA modes for small wave vector \mathbf{q} (resides near the Γ point), indicating intravalley scattering. This observation underscores

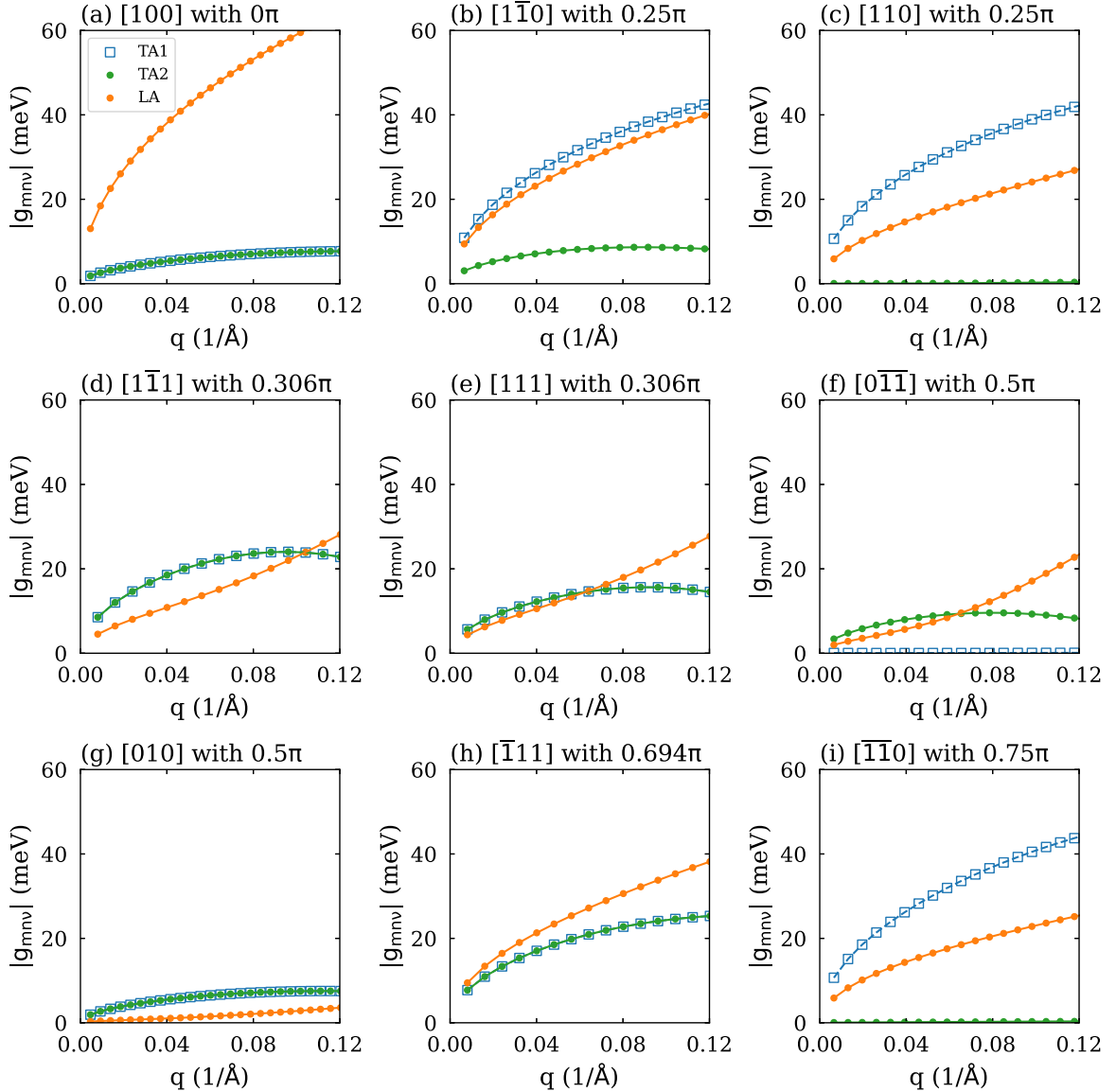


FIG. 6. Intravalley scattering matrix elements $|g_{mnv}(\mathbf{k}, \mathbf{k} + \mathbf{q})|$ for electrons in the conduction band of Si against the phonon wave vector \mathbf{q} along (a) $[100]$, (b) $[1\bar{1}0]$, (c) $[110]$, (d) $[1\bar{1}\bar{1}]$, (e) $[111]$, (f) $[0\bar{1}\bar{1}]$, (g) $[010]$, (h) $[\bar{1}\bar{1}1]$, and (i) $[\bar{1}\bar{1}0]$ directions with $\theta = 0, 0.25, 0.36, 0.5, 0.694, 0.75, \text{ or } 1.0\pi$. The initial electron state $|n, \mathbf{k}\rangle$ is located at one Δ valley, whereas the corresponding final states are $|n, \mathbf{k} + \mathbf{q}\rangle$ within the same Δ valley.

a strong interaction between electrons and long-wavelength LA phonons, consistent with the findings reported in recent literature [13,52]. However, when considering alternative directions, as depicted in Fig. 5(b), a compelling and strong interaction between electrons and TA phonons emerges. This interaction is responsible for the unexpected and substantial contribution of the TA mode to intravalley scattering obtained from the first-principles computations (see Fig. 2).

Furthermore, the scattering matrix elements exhibit anisotropy across various directions. We turn to examine the orientation dependence of the e-ph scattering matrix elements $|g_{mnv}|$ for the long-wavelength limit ($q \rightarrow 0$) since $|g_{mnv}|$ is high anisotropy with respect to the angle θ between phonon wave vector \mathbf{q} and the main axis of the specified valley \mathbf{k} [9]. Setting the longitudinal axis of the $[100]$ valley as the

main axis, we calculate scattering matrix elements along 26 distinct \mathbf{q} directions in the BZ. These directions encompass six $\langle 100 \rangle$ orientations, 12 $\langle 110 \rangle$ orientations, and eight $\langle 111 \rangle$ orientations, thereby yielding θ values of $0, 0.25, 0.36, 0.5, 0.694, 0.75, \text{ and } 1.0\pi$. Figure 6 shows the intravalley scattering matrix element $|g_{mnv}|$ in 9 out of 26 \mathbf{q} directions (the results for the remaining directions align closely with these nine instances). One can observe a remarkable anisotropy in the intravalley scattering matrix elements. Specifically, along the $[100]$ direction, the LA mode has a much larger scattering matrix element than that of the TA modes as expected, whereas along other directions, one of the two TA modes (denoted as TA1 and TA2) alternately exhibits a strong scattering matrix element comparable with the LA mode, with another having a vanishing scattering matrix element. On average, we

can deduce that the TA mode contributes significantly, on par with the LA mode, to the total intravalley scattering.

b. Intervalley scattering matrix elements. Figure 5(a) shows that the scattering matrix element of LO phonons in g -type intervalley scattering becomes finite as the phonon wave vector \mathbf{q} moves away from the Γ point along the Γ - X direction, which is aligned with the selection rules discussed above. The LO mode has the largest scattering matrix element among all phonon modes, exhibiting the predominant role of the LO phonon mode governing the g -type intervalley scattering. This result validates the highest scattering rate from the LO mode as shown in Fig. 2(c), which supports the arguments made in some literature [3,45,47] but also challenges the viewpoints stated in other literature [46,53]. The latter argues that only the LA phonons could scatter electrons from one valley to its opposite valley in the g -type intervalley scattering process. Yu and Cardona [3], in their textbook, also suggested that the LA mode should play a significant role in g -type scattering regarding the LA phonons with an energy of 16 meV, which must be included to reproduce the experimentally measured temperature dependence of the electron mobility in Si.

Figure 5(b) shows the scattering matrix element of Σ phonons for f -type intervalley scattering since the involved phonons in f -type intervalley scattering are mainly from the Σ phonons, located along the Γ - K direction. In the proximity of the f point, the scattering matrix elements of LA, TO, and LO phonons exhibit finite values, and TO phonons have the largest matrix elements, followed by LA phonons, whereas the f -type intervalley matrix elements of TA phonons tend to be zero. These results are consistent with the phonon-decomposed scattering rates predicted by first-principles calculations, as shown in Fig. 2(d). Regarding the LO phonons being symmetry forbidden in the zero-order f -type scattering, the observed finite scattering of the LO phonons should be caused by a first-order scattering process [54], which has been discussed above.

4. Extracting the deformation potential constants for electrons

In the phenomenological e-ph scattering models, the e-ph scattering matrix elements are determined by the adjustable deformation potential constants, which may give rise to incorrect assignment of scattering channels due to their nonunique solutions. It is thus interesting to extract these deformation potential constants directly from the first-principles calculations of the e-ph scattering matrix elements. Such treatment not only facilitates an insightful perspective into the observed phenomenon but also provides insights into the historic underestimation of the TA mode. The deformation potential constants can be extracted from the first-principles calculation of e-ph scattering matrix elements through the following relationship [18,30,55]:

$$D_{mnv}(\mathbf{k}, \mathbf{k} + \mathbf{q}) = \sqrt{\frac{2M_0\omega_{v\mathbf{q}}}{\hbar}} g_{mnv}(\mathbf{k}, \mathbf{k} + \mathbf{q}). \quad (11)$$

Generally, the OP deformation potential constant Ξ_{ODP} defined in Eq. (9) and intervalley deformation potential constants Ξ_{ij} defined in Eq. (10) can be directly obtained through Eq. (11). Note that OP phonons are forbidden in intravalley scattering, and thus, the corresponding OP deformation po-

tential constants are zero. Table III summarizes the extracted intervalley deformation potential constants and corresponding phonon energies for all phonons participating in both g - and f -type intervalley scatterings in Si in comparison with available data reported in the literature [3,6,13,36,56]. Specifically, it exhibits that our extracted LO deformation potential constant for g -type scattering is 3.3 eV, which is within the range of 3–11 eV quoted in the literature [3,6,13,36,56], whereas our extracted LA deformation potential constant is only 0.04 eV, which is an order of magnitude smaller than that commonly quoted in the literature [6]. Therefore, the deformation potential constant of the LA mode is significantly overestimated relative to the LO mode, leading to the common perception that the LA mode predominates g -type intervalley scattering over other phonon modes, including the LO mode [3]. Table III also gives the extracted deformation potential constants and corresponding phonon energies for f -type intervalley scattering. Note that, to the best of our knowledge, the LO deformation potential constants for f -type intervalley scattering have not been given in the literature, but Adachi [36] suggested a range from 0.15 to 4.0 eV. Our extracted LO deformation potential constant of 1.0 eV falls within the suggested range by Adachi [36]. Table III shows that our extracted deformation potential constants of other phonon modes are also in reasonable agreement with the literature. It is worth stressing that the fourfold degeneracy leads to f -type intervalley scattering being four times stronger than g -type scattering even though the deformation potentials in f - and g -type intervalley scattering are comparable in magnitude.

For long-wavelength AC intravalley scattering, the angular-dependent AC deformation potential should be expressed by $\Xi_{v=ac}(\mathbf{k}, \theta) = \lim_{\mathbf{q} \rightarrow 0} | \frac{D_{mnv}(\mathbf{k}, \mathbf{k} + \mathbf{q})}{q} |$ (here, θ is the angle between the phonon wave vector \mathbf{q} and the principal axis of the valley) [6,13]. Thus, the deformation potentials $\Xi_{\text{LA}}(\mathbf{k}, \theta)$ and $\Xi_{\text{TA}}(\mathbf{k}, \theta)$ related to LA and TA modes are equal to $\Xi_{v=ac}(\mathbf{k}, \theta)$ when the phonon mode v corresponds to the LA and TA modes, respectively. According to the theory of Herring and Vogt [4,6,9,12], the effective deformation potentials for the LA mode and the sum of two TA modes are expressed as

$$\Xi_{\text{LA}}(\theta) = \Xi_d + \Xi_u \cos^2 \theta, \quad (12a)$$

$$\Xi_{\text{TA}}(\theta) = \Xi_u \sin \theta \cos \theta. \quad (12b)$$

Here, Ξ_d represents the hydrostatic deformation potential constant, and Ξ_u denotes the uniaxial shear deformation potential constant. The ratio of Ξ_u and Ξ_d reflects the relative strength of the TA and LA scattering channels. We can now deduce Ξ_d and Ξ_u by fitting the θ -dependent $\Xi_{\text{LA}}(\theta)$ and $\Xi_{\text{TA}}(\theta)$ to that obtained from first-principles calculations according to Eqs. (12a) and (12b). In doing so, we first compute scattering matrix elements $g_{mnv}(\mathbf{k}, \mathbf{k} + \mathbf{q})$ employing the first-principles approach and then get the deformation potential $D_{mnv}(\mathbf{k}, \mathbf{k} + \mathbf{q})$ along various directions utilizing Eq. (11). Subsequently, the AC deformation potential D_{ac} is deduced by considering the slope of $D_{mnv}(\mathbf{k}, \mathbf{k} + \mathbf{q})$ with respect to $|\mathbf{q}|$ in the limit of the long-wavelength approximation. This approach yields $\Xi_{\text{LA}}(\theta)$ when the phonon mode v corresponds to the LA mode, and $\Xi_{\text{TA}}(\theta)$ when v pertains to the TA mode.

TABLE III. Intervalley phonon energies (ω) and their deformation potentials in Si. NA stands for not available.

Phonon mode		g-type		f-type	
		ω (meV)	DPs (eV/Å)	ω (meV)	DPs (eV/Å)
TA	Literature	12 ^a	0.5 ^a	19 ^a	0.3 ^a
	This paper	12.33	0.14	20.43	0.06
LA	Literature	18.5 ^a , 22.7 ^a	0.8 ^a	46.67 ^b , 47.3 ^c , 45 ^d , 47.4 ^a	1.83 ^b , 3.4 ^b , 2.51 ^c , 2 ^a
	This paper	21.53	0.04	46.66	1.36
TO	Literature	NA	NA	56.4 ^b , 57.2 ^c , 57 ^d , 59 ^a	3.55 ^b , 2 ^{ab} , 4.44 ^c
	This paper	60.30	0.5	57.96	3.52
LO	Literature	61.06 ^b , 61.6 ^c , 63 ^d , 61.2 ^a	3.86 ^b , 11 ^b , 3 ^b , 4.73 ^b , 3-11 ^c , 11 ^a	NA	NA
	This paper	62.33	3.32	48.02	1.00

^aReference [6]; ^bReference [13]; ^cReference [56]; ^dReference [3].

According to Eq. (12a), $\Xi_{LA}(\theta)$ approximates Ξ_d when $\theta = 0.5\pi$, and a fitting procedure is applied to four distinct directions characterized by $\theta = 0.5\pi$ (namely, [010], [0 $\bar{1}$ 0], [001], and [00 $\bar{1}$] directions) essentially due to the inherent anisotropy of $D_{m\nu}(\mathbf{k}, \mathbf{k} + \mathbf{q})$. We follow this fitting process to obtain $\Xi_d = 0.8$ eV. In parallel, Ξ_u is extracted from $\Xi_{TA}(\theta)$, which holds a nonzero value only for θ deviating from 0, $\pi/2$, and π , according to Eq. (12b). We obtain $\Xi_u = 9.0$ eV by fitting to directions with θ values of 0.25, 0.306, 0.694, and 0.75π .

A comparison of our extracted Ξ_d and Ξ_u from first-principles calculations, with the sets of values reported in existing literature for Si [3,6,12,14,36,57,58], is presented in Table IV. Our deduced $\Xi_u = 9.0$ eV is very close to that commonly quoted in the literature [13,14], whereas our deduced $\Xi_d = 0.8$ eV is an order of magnitude smaller than the values quoted in the literature [3,6,12,36,57,58]. The ratio of $\Xi_u/\Xi_d = 11.4$ according to our deduced potential constants is approximately an order of magnitude larger than that from most literature, with the exception of Refs. [13,14], explaining why the TA mode was usually regarded as negligible in an e-ph scattering [6,8] since it is a pivotal factor in determining the relative importance of TA and LA modes in intravalley scattering. Note that Fischetti and Laux [14] obtained $(\Xi_u, \Xi_d) = (10.5, 1.1)$ eV with the ratio $\Xi_u/\Xi_d = 9.5$, which are in remarkable proximity to our results extracted from first-principles calculations by simultaneously fitting electron and hole mobilities to experimental data to avoid uncertainties.

We next proceed to disclose how Ξ_u and Ξ_d determine the relative importance of LA and TA to intravalley scattering, relying on the Herring-Vogt relation [Eqs. (12a) and (12b)]. Figure 7(a) shows the θ -dependent deformation potentials $\Xi_{LA}(\theta)$ and $\Xi_{TA}(\theta)$ based on two frequently cited sets of deformation potential constants $(\Xi_u, \Xi_d) = (10, -11.5)$ and $(8.3, 5.0)$ eV [6,57,58] according to Eqs. (12a) and (12b). Both sets of (Ξ_u, Ξ_d) constants give rise to $\Xi_{LA}(\theta)$ much larger than $\Xi_{TA}(\theta)$, especially within the angular range of $\theta = \pi/2$ (spanning from $\pi/4$ to $3\pi/4$). This angular segment plays a paramount role in intravalley scattering as restricted by the conservation laws of momentum and energy. Therefore, the TA mode is commonly thought to be negligible in determining the electron mobility in Si [6,8], whereas corresponding results obtained from our first-principles calculations are shown in Fig. 7(b). Remarkably, the TA and LA deformation potentials $\Xi_{TA}(\theta)$ and $\Xi_{LA}(\theta)$ obtained from the Herring-Vogt relation using the extracted $\Xi_d = 0.8$ eV and $\Xi_u = 9.0$ eV reproduce well those directly obtained from first-principles calculations over a wide span of angular values. This good agreement underscores the robustness of the fitting procedure employed to extract deformation potential constants. Interestingly, it exhibits that the LA deformation potential $\Xi_{LA}(\theta)$ undergoes a significant reduction, approaching $\Xi_{TA}(\theta)$, within the angle range of $\pi/4$ to $3\pi/4$. In proximity to $\theta = \pi/2$, $\Xi_{TA}(\theta)$ is even larger than $\Xi_{LA}(\theta)$, illustrating the substantial contribution of the TA mode to the intravalley scattering.

TABLE IV. Comparison of the intravalley deformation potentials for electrons in Si quoted in the literature and our extracted values from the first-principles calculation.

	Ξ_d (eV)	Ξ_u (eV)	Ξ_u/Ξ_d
Yu and Cardona, 2010 ^a and Blacha <i>et al.</i> , 1984 ^b	5.0	8.3	1.7
Ridley, 2013 ^c and Neuberger, 1971 ^d	-6.0	7.8, 9.2	1.3 or 1.5
Hamaguchi, 2017 ^e	-11.5, 5	10.0, 9.2	0.9, 1.8
Fischetti and Laux, 1996 ^f	-10.7, 1.1	8.86, 9.2, 7.3, 10.5	9.5
Adachi, 2006 ^g	2.9	8.6	3.0
This paper	0.8	9.0	11.4

^aReference [3]; ^bReference [57]; ^cReference [12]; ^dReference [58]; ^eReference [6]; ^fReference [14]; ^gReference [36].

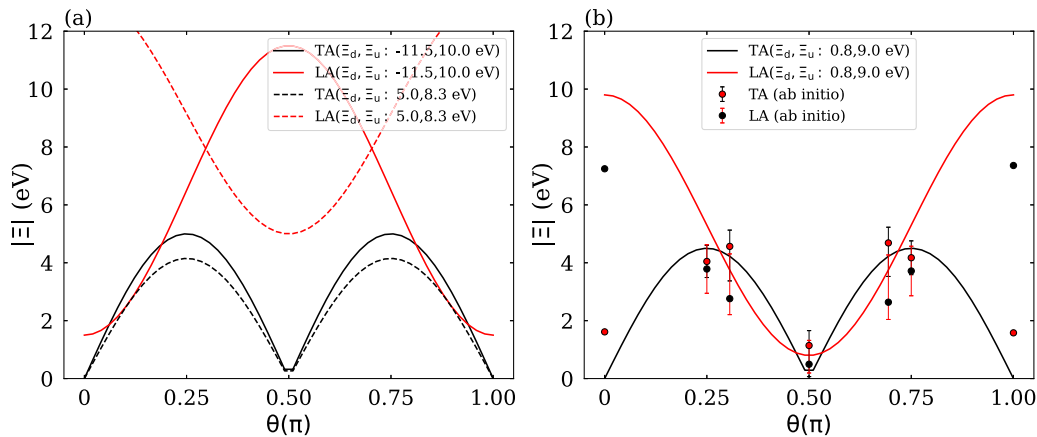


FIG. 7. Comparison of the deformation potentials for intravalley scattering of electrons in Si as a function of angle θ between the phonon wave vector \mathbf{q} and the principal axis of the valley. The θ dependence of effective transverse acoustic (TA) and longitudinal acoustic (LA) deformation potentials obtained from the theory of Herring and Vogt [4,6,9,12] according to Eqs. (12a) and (12b) by setting constants Ξ_u and Ξ_d of the hydrostatic deformation potential and uniaxial shear deformation potential to (a) $(\Xi_u, \Xi_d) = (10.0, -11.5)$ eV and $(\Xi_u, \Xi_d) = (8.3, 5.0)$ eV, which are two sets frequently quoted in the literature [6,57,58], and (b) our extracted $(\Xi_u, \Xi_d) = (0.8, 9.0)$ eV from the first-principles calculation-predicted TA (marked by red dots) and LA deformation potentials (marked by black dots). Note that the TA deformation potential is a sum of two TA modes.

C. Phonon-limited scattering for holes in Si

1. Hole-phonon scattering rates

Figure 8 shows the hole-phonon scattering rates in Si at the temperature of 300 K. Different from electrons occupying the Δ valley of the conduction bands, holes occupy the Γ valley of the valence bands, which are fourfold degenerate

at the Γ point (zone center) and split into heavy-hole (hh) and light-hole (lh) bands away from the Γ point. Phonons have no sufficient energy to scatter holes from the Γ valley to other valleys since their energy separation is in several eV, but phonons can scatter holes from hh to hh (so-called intraband scattering) or from hh to lh or from lh to hh (so-called interband scattering) within the Γ valley, as schematically

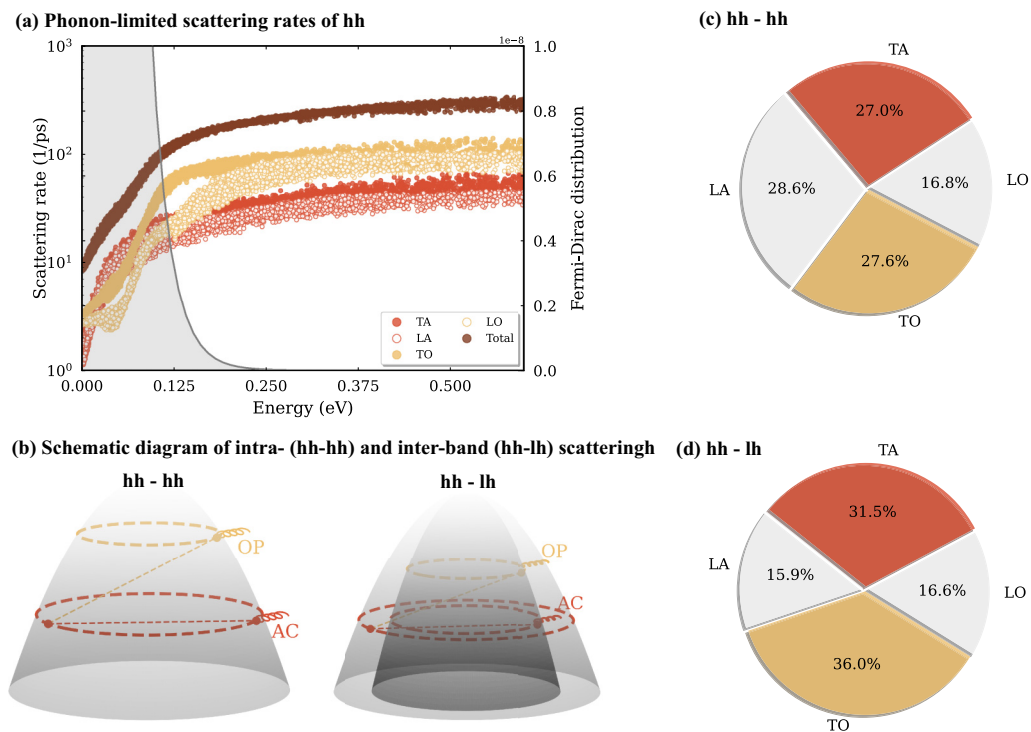


FIG. 8. (a) Heavy hole (hh) scattering rate decomposed into different phonon branches with respect to different electron energies from the band extrema at 300 K. (b) Schematic diagram of intraband and interband scattering induced by acoustic (AC) and optical (OP) phonons for hh. Pie chart representation of the proportion of average electron scattering rate induced by different phonon-limit scattering channels (c) to hh intraband scattering and (d) interband scattering from hh to light hole (lh) band. Here, the transverse modes consider both branches.

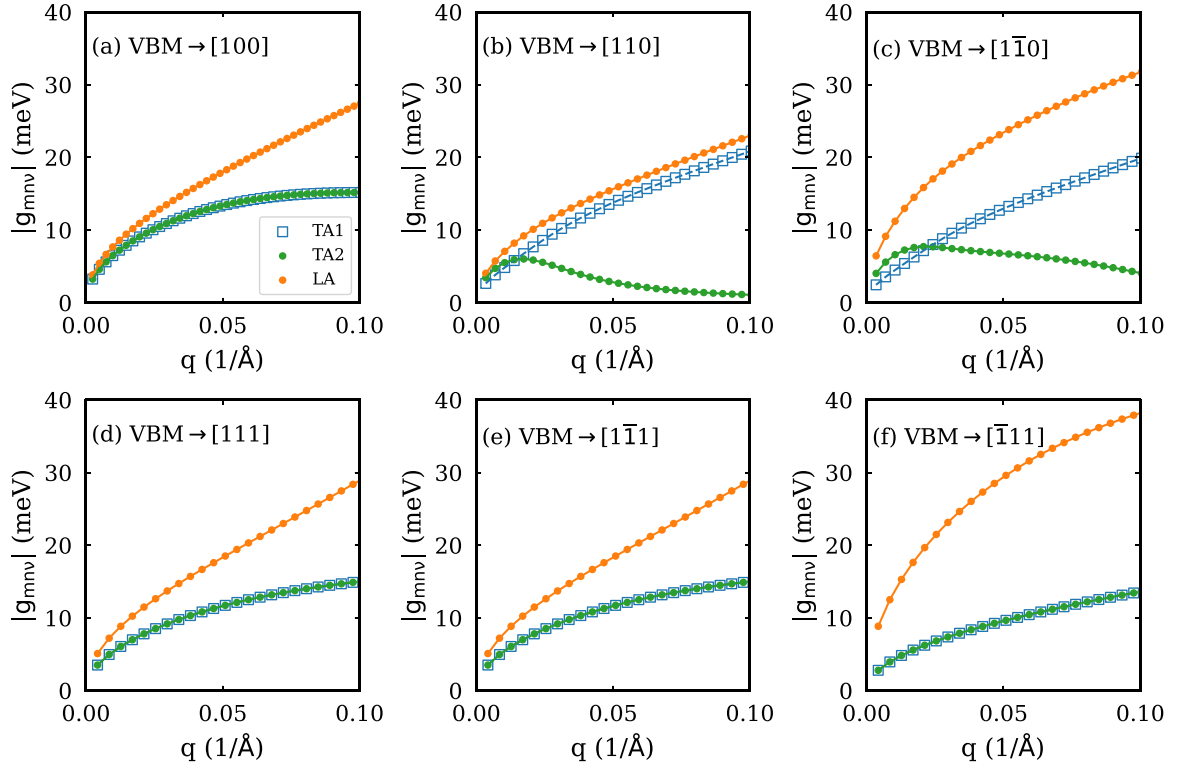


FIG. 9. Hole-phonon scattering matrix elements $g_{mnv}(\mathbf{k}, \mathbf{k} + \mathbf{q})$ in Si for a hole initially located at the valence band maximum (VBM; heavy hole [hh] band) transition to the hh band (intraband scattering) as a function of the phonon momentum \mathbf{q} along (a) [100], (b) [110], (c) $[1\bar{1}0]$, (d) [111], (e) $[1\bar{1}\bar{1}]$, and (f) $[\bar{1}\bar{1}1]$ directions. Since optical phonons are forbidden by symmetry in the hole-phonon scattering, here, we only show the acoustic phonon scattering matrix elements for two transverse acoustic (TA) modes (denoted as TA1 and TA2) and one longitudinal acoustic (LA) mode.

diagramed in Fig. 8(b). Figure 8(a) shows the phonon-limited hole scattering rates as a function of hole energy $\varepsilon_{hh,\mathbf{k}}$ for a hole initially located at the hh band and wave vector \mathbf{k} in Si. It can be further divided into intraband and interband scatterings. Specifically, Fig. 8(c) displays the contribution of each phonon mode to the intraband scattering of a hole from hh band to hh band (hh-hh), and Fig. 8(d) displays the interband scattering from hh band to lh band (hh-lh). In the low-energy region ($\varepsilon_{hh,\mathbf{k}} < 0.05$ eV), AC-phonon scattering is slightly stronger than OP-phonon scattering, and their transversal components (TA and TO) are stronger than their longitudinal components (LA and LO). With increasing the energy, OP-phonon scattering rises at a much faster rate than AC-phonon scattering and then becomes predominant over AC-phonon scattering in the high-energy region ($\varepsilon_{hh,\mathbf{k}} > 0.1$ eV). However, the contribution of AC-phonon scattering is comparable with that of OP-phonon scattering, as shown in Figs. 8(c) and 8(d). This is because most of the holes are in the low-energy region at room temperature according to the Fermi-Dirac distribution [Fig. 8(a)]. Interestingly, we again find that TA phonons contribute remarkably to hh-hh intraband scattering in a similar role as LA phonons, as shown in Fig. 3(c). In hh-lh interband scattering, the contribution of TA phonons is further increased to the extent that it is twice that of the LA phonons, as shown in Fig. 8(d). It is in contrast to the common belief that TA phonons are negligible in the hole-phonon scattering [6,10,15,42]. For instance, Hamaguchi [6] and Gantmakher and Levinson [42] emphasized that hole

mobility depends strongly on the interaction between holes and LA phonons. Ehrenreich [10] underlined that LA scattering is stronger than TA scattering within a given valence band (intraband scattering), whereas both types are equally significant in interband scattering. Madarasz and Szmulowicz [15], based on a multiband model calculation, also illustrated that the contribution of the LA phonons to hole-phonon scattering is significantly greater than that of two TA modes in both hh intraband and interband scatterings. Li *et al.* [13] also neglected the contribution of TA phonons in the analysis of first-principles calculations of hole mobility in Si with the argument that AC-phonon scattering of holes exclusively arises from LA phonons since the dilation component (associated only with the LA mode) of the AC-phonon-induced strain holds a role of greater importance than the shear components (associated with both LA and TA modes) in the deformation potential scattering for holes [3,8,13].

2. Selection rules for hole-phonon scattering

In diamond-type Si, the VBM located at the zone-center Γ point is derived from threefold degenerate p states and belongs to the Γ_5^+ (T_{2g}) irreducible representation of the O_h group without considering spin-orbit coupling. Due to the holes being in the single Γ valley, which is far away from the L and X valleys in energy, intervalley scattering is negligible for holes. The direct product of the initial and final states in

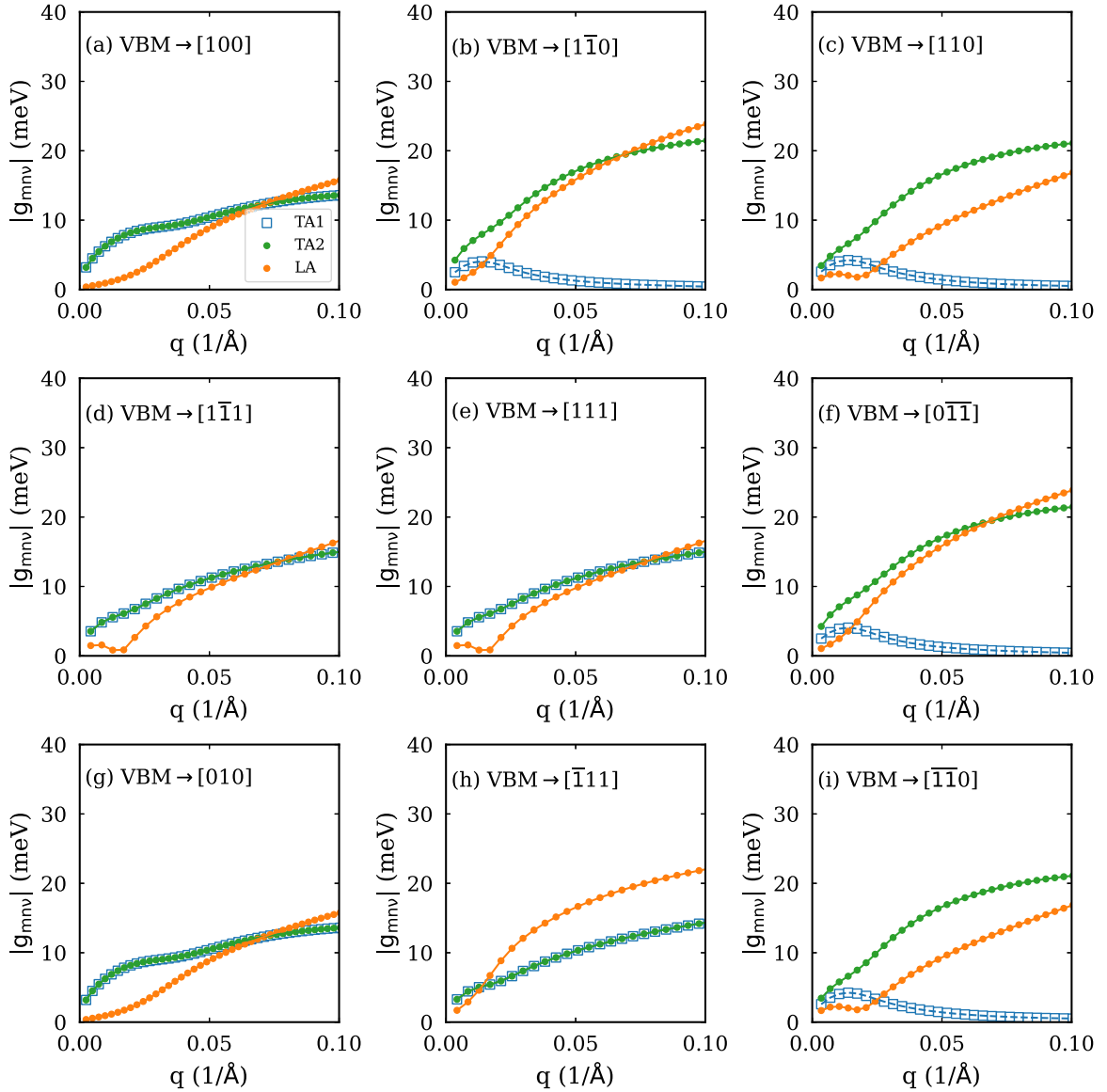


FIG. 10. (a)–(i) Hole-phonon scattering matrix elements $g_{mnv}(\mathbf{k}, \mathbf{k} + \mathbf{q})$ for the transition of holes in Si from the heavy hole (hh) band to the light hole (lh) band as a function of the phonon momentum q .

hole-phonon scattering is expressed by

$$T_{2g} \otimes T_{2g} = A_{1g} \oplus E_g \oplus T_{2g}. \quad (13)$$

The energy and momentum conservation laws restrict hole-phonon scattering to long-wavelength modes, and thus, the hole-phonon interaction Hamiltonian is the combination of H_{ADP} [Eq. (8)] for AC phonons and H_{ODP} [Eq. (9)] for OP phonons. The AC-phonon-strain Hamiltonian H_{ADP} has a symmetry of $A_{1g} \oplus E_g \oplus T_{2g}$ with the LA component belonging to $A_{1g} \oplus E_g \oplus T_{2g}$ and TA components to $E_g \oplus T_{2g}$. The scattering matrix elements are nonzero for both LA and TA modes, whereas the OP-phonon-strain Hamiltonian H_{ODP} has a symmetry of T_{2g} with LO and TO modes degenerate at the Γ point. The scattering matrix elements are also nonzero for both LO and TO modes. Therefore, all LA, TA, LO, and TO phonon modes are allowed for hole-phonon scattering, as given in Table II.

3. First-principles calculations of scattering matrix elements for holes in Si

Figure 9 shows the matrix elements of holes scattering from the VBM to a final state at \mathbf{q} along various directions by LA and TA (two TA modes are denoted as TA1 and TA2) mode phonons for hh-hh intraband transitions. More details for hh-lh interband transitions have been displayed in Fig. 10. Specifically, Fig. 9(a) displays that the scattering of holes by the TA mode is unexpectedly finite and so strong that it is only slightly smaller than that of the LA mode, for phonon momentum vector (\mathbf{q}) along the [100] direction. The finding is consistent with earlier first-principles calculations reported in Ref. [52] but in sharp contrast with the classical deformation potential models [15,42,59]. Without taking a reduction from six to four bands for the valence band structure, Bir and Pikus [9,16] demonstrated that the deformation potential matrix element (B_{xy} and B_{xz}) should be finite even for $\theta = 0$. Figure 9(a)

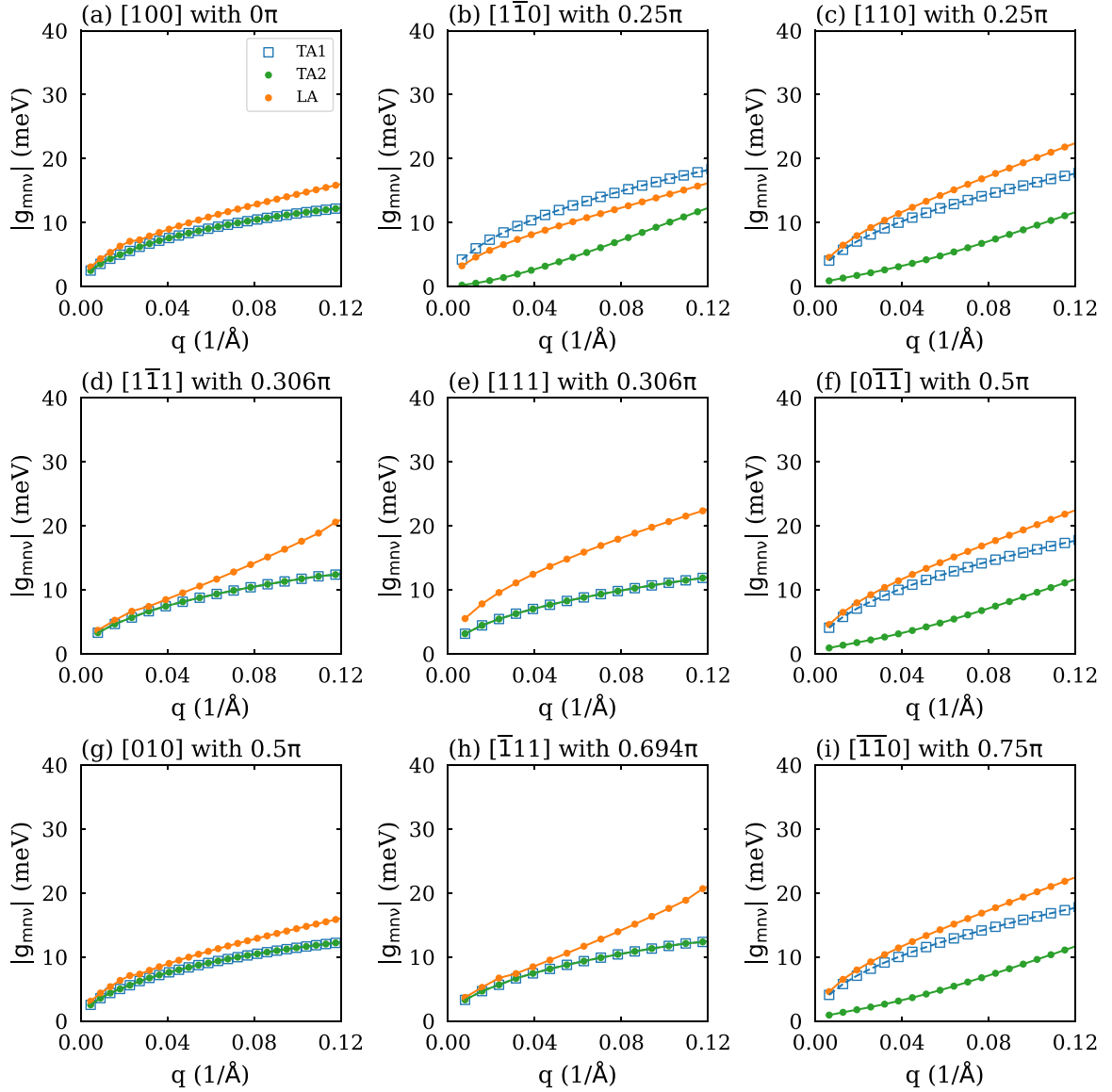


FIG. 11. (a)–(i) Hole-phonon scattering matrix elements $g_{mnv}(\mathbf{k}, \mathbf{k} + \mathbf{q})$ for the transition of holes in GaAs from the heavy hole (hh) band to the hh band as a function of the phonon momentum \mathbf{q} .

also shows that the scattering matrix elements of two TA modes are degenerate, as expected. However, Figs. 9(b) and 9(c) show that the degeneracy of the scattering matrix elements of two TA modes is lifted for phonons along the [110] and $[1\bar{1}0]$ directions, and TA1 mode scattering probability diminishes gradually and eventually becomes negligible, but TA2 scattering probability raises in the same trend as the LA mode as the phonon momentum away from the zone center. Hole-phonon scattering is different along [110] and $[1\bar{1}0]$ directions, which are equivalent in the valence band structure, implying a high anisotropy in hole-phonon scattering. For \mathbf{q} along eight equivalent $\langle 111 \rangle$ directions, Figs. 9(d)–9(f) show that the hole-phonon scattering of two TA modes is degenerate but nonequivalent between these eight equivalent directions. This high anisotropy in hole-phonon scattering questions the validity of the classical models with an isotropic phonon assumption [15,42,59]. We can safely conclude that our results uncover a significant role of TA modes in hole-phonon scat-

tering for Si. This conclusion is also applicable to compound semiconductors, as shown in Figs. 11–12 for GaAs as a representative example.

Considering the strong angular dependence of hole-phonon scattering matrix elements within the classical deformation potential model [42], we proceed to examine it based on first-principles calculations. Considering a hole initially located at a state along the [100] direction in close proximity to the VBM, we calculate the scattering matrix elements by TA and LA modes as a function of scattering angle θ . Figure 13 shows the averaged hole-phonon scattering matrix elements by LA (red dots) and TA (black dots for a sum of TA1 and TA2) modes, respectively. The error bars indicate the range of scattering matrix elements at the same scattering angle but in different directions, reflecting the anisotropic properties of hole-phonon scattering. Hole-TA-phonon scattering is remarkably strong even at $\theta = 0$ and π rather than vanishing, as obtained in the classical models, which take an assumption

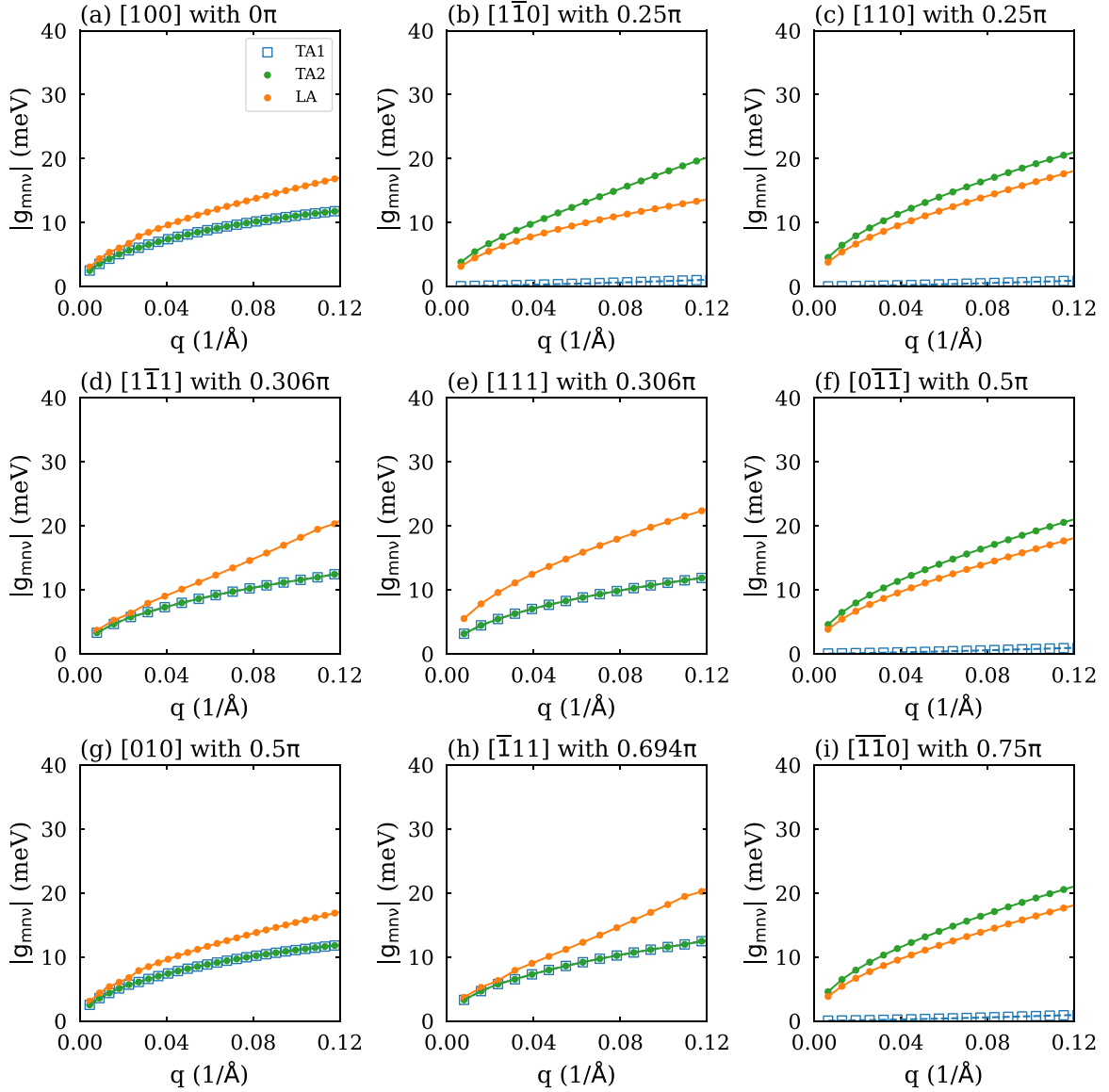


FIG. 12. (a)–(i) Hole-phonon scattering matrix elements $g_{mnv}(\mathbf{k}, \mathbf{k} + \mathbf{q})$ for the transition of holes in GaAs from the heavy hole (hh) band to the light hole (lh) band as a function of the phonon momentum q .

of isotropic phonons. The scattering matrix elements of LA and TA modes are in high overlap and are insensitive to the scattering angle, in sharp contrast to the classical models. At $\theta = \pi/2$, two TA modes give an even stronger scattering than the LA mode. These results explain why we can obtain a significant contribution of TA mode scattering (in a magnitude comparable with LA mode scattering) to the hole mobility from first-principles calculations, as shown in Fig. 8.

4. Extracting the deformation potential constants for holes

We now turn to directly extracting the deformation potential constants from first-principles calculations of hole-phonon scattering matrix elements. Although the significant role of the TA phonons in hole-phonon scattering has been underestimated remarkably in the classical deformation potential models, we can still extract the deformation potential

constants from first-principles calculations of hole-phonon scattering based on a simplification by combining the contributions of LA and TA modes to hole-phonon scattering into total AC scattering in an isotropic band model for hole scattering [6,14,16,60]. According to Lawaetz [16], total AC scattering can be described by the same single deformation potential constant $|\Xi_{\text{eff}}|$ for all types of transitions with $|\Xi_{\text{eff}}|$ defined as follows:

$$|\Xi_{\text{eff}}|^2 = \frac{\beta + 2}{3\beta} \cdot \left[a^2 + \beta \left(b^2 + \frac{1}{2} d^2 \right) \right]. \quad (14)$$

Here, β is the ratio of the longitudinal (c_l) to transverse (c_t) elastic constants and is ~ 2.86 for Si [13,35]. It has been established that this effective deformation potential constant is related to the LA and TA scattering matrix elements through $|\Xi_{\text{eff}}|^2 = \frac{\beta+2}{3\beta} [\Xi_{\text{LA}}^2 + \beta \Xi_{\text{TA}}^2]$ [13], where $\Xi_{\text{LA}}^2 = a^2$ and $\Xi_{\text{TA}}^2 = (b^2 + \frac{1}{2} d^2)$ by neglecting the shear components

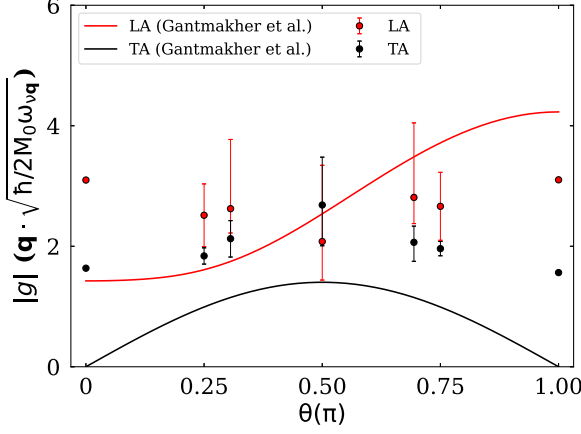


FIG. 13. Comparison of angular-dependent hole-phonon scattering matrix elements $|g|$ obtained from the classic deformation model [42] (solid lines) and from the first-principles calculations (dots with error bar) for intraband transitions by longitudinal acoustic (LA) and transverse acoustic (TA) modes.

of the LA mode. If we learn Ξ_{TA} and Ξ_{TA} , we can thus obtain Bir-Pikus deformation potentials a , b , and d utilizing the empirical relationship $d/\sqrt{3}b = 1.39f_i + 1.1$ (here, f_i is the Phillips ionicity) proposed by Adachi [36]. To account for the

nonparabolic property of the band in the multiband model (i.e., valence bands), Gantmakher and Levinson [42] developed a formula to connect Ξ_{LA} and Ξ_{TA} with angular-dependent deformation potentials $\Xi_{LA}^{m \rightarrow n}(\theta)$ and $\Xi_{TA}^{m \rightarrow n}(\theta)$, respectively:

$$|\Xi_{LA}^{m \rightarrow n}(\theta)|^2 = |\Xi_{LA}|^2 |G_{mn}(\theta)|^2, \quad (15a)$$

$$|\Xi_{TA}^{m \rightarrow n}(\theta)|^2 = |\Xi_{TA}|^2 |G_{mn}(\theta)|^2. \quad (15b)$$

Here, $|G_{mn}(\theta)|^2 [\approx \frac{1}{4}(1 + 3 \cos^2 \theta)$ for intraband transitions and $\frac{3}{4} \sin^2 \theta$ for interband transitions] are the overlap factors between the periodic parts of the initial and final Bloch states, which have been calculated analytically by Costato and Reggiani [61] and Gantmakher and Levinson [42]. The angular-dependent LA and TA deformation potentials $\Xi_{LA}^{m \rightarrow n}(\theta)$ and $\Xi_{TA}^{m \rightarrow n}(\theta)$ can be obtained through the relationship $\Xi_v^{m \rightarrow n}(\theta) = \lim_{q \rightarrow 0} |D_{mv}(\mathbf{k}, \mathbf{k} + \mathbf{q})|$ (setting $v = TA$ and LA phonon modes, respectively) by deriving deformation potential matrix elements $|D_{mv}(\mathbf{k}, \mathbf{k} + \mathbf{q})|$ from $|g_{mv}(\mathbf{k}, \mathbf{k} + \mathbf{q})|$ according to Eq. (11). Table V summarizes the extracted $\Xi_{LA}^{m \rightarrow n}(\theta)$ and $\Xi_{TA}^{m \rightarrow n}(\theta)$ for hh-hh intraband ($m, n = hh$) scattering and hh-lh interband ($m = hh, n = lh$) scattering. Once we learn the angular-dependent deformation potentials, we can obtain deformation potentials Ξ_{LA} and Ξ_{TA} according to Eqs. (15a) and (15b). It is straightforward to finally gain the Bir-Pikus deformation potential constants

TABLE V. Intraband (hh \rightarrow hh) and interband (hh \rightarrow lh) AC deformation potentials (in units of eV) related to hole-TA-phonon and hole-LA-phonon coupling in Si along different directions of \mathbf{q} with $\mathbf{q} \rightarrow \mathbf{0}$.

Direction	$\theta(\pi)$	Intraband		Interband	
		$ \Xi_{hh \rightarrow hh}^{TA}(\theta) $	$ \Xi_{hh \rightarrow hh}^{LA}(\theta) $	$ \Xi_{hh \rightarrow lh}^{TA}(\theta) $	$ \Xi_{hh \rightarrow lh}^{LA}(\theta) $
[100]	0	1.614	7.247	0.057	0.008
[1 $\bar{1}$ 0]	0.25	4.6	4.625	3.57	0.126
[110]	0.25	3.491	2.946	3.624	0.044
[10 $\bar{1}$]	0.25	4.6	4.625	3.569	0.125
[101]	0.25	3.491	2.946	3.627	0.044
[1 $\bar{1}$ $\bar{1}$]	0.306	4.632	4.306	3.796	2.948
[1 $\bar{1}$ 1]	0.306	5.128	2.263	3.609	3.224
[11 $\bar{1}$]	0.306	5.128	2.263	3.608	3.224
[111]	0.306	3.374	2.209	3.36	3.258
[0 $\bar{1}$ $\bar{1}$]	0.5	1.201	1.226	0.48	4.957
[0 $\bar{1}$ 1]	0.5	0.068	0.304	0.131	5.103
[01 $\bar{1}$]	0.5	0.068	0.304	0.127	5.103
[011]	0.5	1.187	1.319	0.052	4.934
[010]	0.5	1.657	0.211	7.153	0.035
[0 $\bar{1}$ 0]	0.5	1.649	0.193	7.141	0.045
[001]	0.5	1.657	0.211	7.153	0.027
[00 $\bar{1}$]	0.5	1.649	0.193	7.141	0.033
[$\bar{1}$ $\bar{1}$ $\bar{1}$]	0.694	3.527	2.041	3.192	3.506
[$\bar{1}$ $\bar{1}$ 1]	0.694	5.228	2.12	3.439	3.452
[$\bar{1}$ 1 $\bar{1}$]	0.694	5.228	2.12	3.439	3.452
[$\bar{1}$ 11]	0.694	4.761	4.27	3.724	3.12
[$\bar{1}$ $\bar{1}$ 0]	0.75	3.59	2.861	3.731	0.055
[$\bar{1}$ 10]	0.75	4.757	4.572	3.659	0.024
[$\bar{1}$ 0 $\bar{1}$]	0.75	3.59	2.861	3.731	0.055
[$\bar{1}$ 01]	0.75	4.757	4.572	3.654	0.019
[$\bar{1}$ 00]	1	1.58	7.36	0.006	0.12
Average		3.162	2.699	3.337	1.809

TABLE VI. Bir-Pikus deformation potentials (a , b , and d) extracted from hole-phonon matrix elements predicted by first-principles methods in Si compared with previous experimental and theoretical results. All quantities are in units of eV.

	a (eV)		b (eV)		d (eV)	$ \Xi_{\text{eff}} $ (eV)
This paper	2.36	-1.87			-3.60	4.40
Adachi, 2016 ^a	-5.0	-2.3			-5.3	6.74
Blacha <i>et al.</i> , 1984 ^b	-10.2	-3.5, -2.3			-3.9	9.54, 8.93
Fischetti and Laux, 1996 ^c	2.1	-2.33			-4.75	5.44
Wiley, 1970 ^d	2.1	-1.5			-3.4	3.94
Friedel <i>et al.</i> , 1989 ^e	2.06	-2.27			-3.69	4.67
Li <i>et al.</i> , 2021 ^f						5.48 (for LA)
Ottaviani <i>et al.</i> , 1975 ^g , Gantmakher and Levinson, 1987 ^h	2					2.2
Cardona and Pollak, 1966 ⁱ		-2.58			-5.3	
Others	-9.7 ^c	-2.1 ^j , -2.33 ^k , -2.12 ^l , -2.35 ^m , -2.58 ⁱ			-4.85 ^j , -5.3 ^{im}	5.48 ^f , 5.39 ^c , 5.0 ^{no} , 6.2 ^p , 3.1 ^q

^aReference [36]; ^bReference [57]; ^cReference [14]; ^dReference [62]; ^eReference [63]; ^fReference [13]; ^gReference [65]; ^hReference [42]; ⁱReference [72]; ^jReference [68]; ^kReference [69]; ^lReference [70]; ^mReference [71]; ⁿReference [8]; ^oReference [64]; ^pReference [66]; ^qReference [67].

a , b , and d . The extracted Bir-Pikus deformation potentials a , b , and d scattering matrix elements calculated directly from first-principles methods are summarized in Table VI in comparison with frequently quoted sets of deformation potentials obtained from fitting to the hole mobility of Si [8,14,36,42,57,62–72]. By fitting to hh-hh intraband and hh-lh interband scattering matrix elements, respectively, we obtain two different sets of deformation potentials: one is $a = 3.21$, $b = -1.76$, and $d = -3.37$ eV from hh-hh intraband scattering, and another is $a = 2.36$, $b = -1.87$, and $d = -3.60$ eV, an average of intraband and interband scatterings (presented in Table VI). From Table VI, our extracted average deformation potentials are in good agreement with three sets given by Wiley [62], by Friedel *et al.* [63], and by Fischetti and Laux [14]. The last one has become the benchmark of Si deformation potentials. On the other hand, the overestimated $a = -10.2$ eV [57], -9.7 eV [14], and -5 eV [36] give rise to a pronounced hole-phonon interaction, which leads to an underestimation of hole mobility at 300 K [14]. To check the validity of extracting the deformation potentials (a , b , d) from scattering matrix elements, we calculate the temperature-dependent hole mobility based on the classical model [73] using our deduced sets of deformation potentials, as shown in Fig. 14. We also compare predicted hole mobility with that using the standard set given by Fischetti and Laux [14] and obtained directly from first-principles calculations and experimental measurements [31–33]. Surprisingly, our two extracted sets of deformation potentials can both reproduce the hole mobility in the investigated temperature range very well, even though they have rather different a 's. Their good agreement is due to the fact that they have a similar Ξ_{eff} (4.40 vs 4.49 eV), which is a combination of TA and LA modes and implies the difficulty in correctly distinguishing the contributions of TA and LA modes by fitting to the hole mobility. It is worth mentioning that, in Fig. 14, there are two sets of hole mobilities for a single set of deformation potentials given by Fischetti and Laux [14]: one (solid green

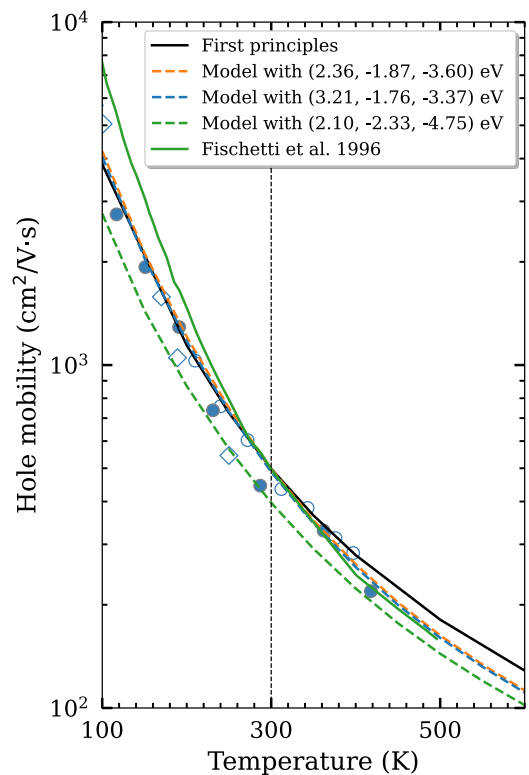


FIG. 14. Comparison of phonon-limited hole mobility in Si as a function of temperature. The black solid line and dots represent hole mobilities predicted by first-principles methods and measured by experiment, respectively, as shown in Fig. (1). Dashed lines represent the predicted hole mobilities by the classical model (see details in Ref. [73]) with deformation potentials (a , b , d) of (2.36, -1.87 , -3.60) eV [orange, fitted from heavy hole (hh) matrix elements], (3.21, -1.76 , -3.37) eV (blue, fitted from hh intraband matrix elements), and (2.1, -2.33 , -4.75) eV (green, obtained by Fischetti and Laux [14]), respectively. The solid green line is the data adopted directly from Ref. [14].

line) is directly adopted from Fig. 9 in Ref. [14], and the other (dashed green line) is calculated also using the classical model but using a $|k|$ -dependent DOS effective mass (see details in Refs. [14,73]). One can note that the hole mobility obtained from Fischetti and Laux [14] is in excellent agreement with experimental data in the high-temperature regime ($T > 250$ K), but a noticeable divergence emerges at lower temperatures. Such a divergence (the overestimation of hole mobility) in low temperatures is caused by the approximation of $|k|$ -independent (although angular-dependent) DOS effective mass since it has a larger $\Xi_{\text{eff}} = 5.44$ eV than our deduced $\Xi_{\text{eff}} = 4.40$ eV.

Our extracted deformation potential constants from first-principles calculations are within the range utilized in classical models, but the latter generally underestimate the role of TA modes. The underlying reason can be addressed from the comparison of hole-phonon scattering matrix elements obtained from the classical models and from our first-principles calculations as discussed above. Specifically, our first-principles calculation yields hole-phonon scattering matrix elements of both TA and LA modes being insensitive to angle θ and comparable with each other in magnitude, as shown in Fig. 13. However, with a set of comparable Bir-Pikus deformation potentials $a = 2.36$, $b = -1.87$, and $d = -3.60$ eV with respect to our extracted set from first-principles calculations, the classical models with an assumption of the isotropic bands give a high angular dependence of hole-TA-phonon scattering matrix elements, which vanishes at $\theta = 0$ and π , and its maximum at $\theta = \pi/2$ is also smaller than that of the LA mode. It implies that the underestimation of the TA mode in hole-phonon scattering by the classical models is embedded in their physics roots with *ad hoc* assumptions.

IV. CONCLUSIONS

In this paper, we have re-examined the e-ph and hole-phonon scattering in Si by conducting first-principles calculations for carrier mobilities. Our predicted electron and hole mobilities are in approximately good agreement with experimental data over a wide range of temperatures even without *ad hoc* adjustable parameters. We demonstrated that the e-ph scattering mechanisms revealed in this paper are dramatically different from what is the common belief established based on classical models involving relying on adjustable parameters. Specifically, we found that TA phonons have a comparable contribution with LA phonons in the scattering of both electrons and holes on limiting the carrier mobilities in Si by decomposition of first-principles calculation-predicted e-ph scattering into the contributions from different phonon modes and electronic valleys. We also revealed that the TO phonon mode, rather than the conventionally presumed LO and LA modes, provides the leading scattering channel (accounting

for 58%) in f -type intervalley scattering, and the LO mode is dominant over the LA mode in g -type intervalley scattering for electrons in Si. It calls for developing a correct semiempirical carrier-phonon scattering model.

Specifically, in the popular three-dimensional (3D) TCAD simulator nextnano, the phonon-limited lattice mobility $\mu_{p,n}^l$ (subscript n indicates electron and p for hole) at room temperature in Si and Ge considering only the interaction with AC phonons is given by [74–76]

$$\mu_{p,n}^l = \frac{\sqrt{8\pi} q \hbar^4 C_l}{3D_{ac}^2 m_c^{*5/2} k_B T^{3/2}}. \quad (16)$$

Here, C_l signifies the average longitudinal elastic constant, D_{ac} represents the deformation potential of the band edge, and m_c^* denotes the conductivity effective mass. The deformation potential D_{ac} in Eq. (16) is determined by fitting $\mu_{p,n}^l(T)$ to experimentally measured values (calibration process) to account for the effects of neglected TA and TO phonons on carrier scattering, which are found to be important in this paper. Furthermore, in the Sentaurus (the Synopsys TCAD tool), the temperature-dependent phonon-limited lattice mobility is even taken as an adjustable parameter for all semiconductors without relying on the detailed scattering processes [77]:

$$\mu_{p,n}^l(T) = \mu_{p,n}^l(T = 300 \text{ K}) \left(\frac{T}{300 \text{ K}} \right)^{-r}, \quad (17)$$

where a power factor r and $\mu_{p,n}^l(T = 300 \text{ K})$ are material-dependent fitting parameters via fitting temperature-dependent mobility to experimental data. With properly calibrated physical models, it is expected that TCAD simulation can accurately model integrated circuit-manufacturing processes and predict the electrical characteristics of fabricated devices. Because it lacks the capability of prediction, the calibration process of TCAD simulators is a crucial step in technology characterization. Our findings indicate that the physical models of phonon-carrier scattering used in the state-of-the-art TCAD device simulation are improperly treated, which hinders the development of predictive TCAD tools.

ACKNOWLEDGMENTS

This paper was supported by the National Key R&D Program of China (Grants No. 2022YFB3604400, No. 2022YFA1402701, and No. 2022YFA1403202), the National Natural Science Foundation of China under Grants No. 61927901, No. 11925407, and No. 12074333, and the Key Research Program of Frontier Sciences, CAS under Grant No. ZDBS-LY-JSC019, CAS Project for Young Scientists in Basic Research under Grant No. YSBR-026, the Strategy Priority Research Program (Category B) of CAS under Grant No. XDB43020000.

[1] W. Shockley and J. Bardeen, Energy bands and mobilities in monatomic semiconductors, *Phys. Rev.* **77**, 407 (1950).

[2] J. Bardeen and W. Shockley, Deformation potentials and mobilities in non-polar crystals, *Phys. Rev.* **80**, 72 (1950).

- [3] P. Y. Yu and M. Cardona, *Fundamentals of Semiconductors: Physics and Materials Properties*, 4th ed., Graduate Texts in Physics (Springer, Berlin, 2010).
- [4] C. Herring and E. Vogt, Transport and deformation-potential theory for many-valley semiconductors with anisotropic scattering, *Phys. Rev.* **101**, 944 (1956).
- [5] H. Fröhlich, Electrons in lattice fields, *Adv. Phys.* **3**, 325 (1954).
- [6] C. Hamaguchi, *Basic Semiconductor Physics*, 3rd ed., Graduate Texts in Physics (Springer International Publishing, Berlin, 2017).
- [7] Z. Shuai, L. Wang, and C. Song, Deformation potential theory, in *Theory of Charge Transport in Carbon Electronic Materials* (Springer, Berlin, 2012), pp. 67–88.
- [8] M. Lundstrom, *Fundamentals of Carrier Transport*, 2nd ed. (Cambridge University Press, Cambridge, 2000).
- [9] G. L. Bir and G. E. Pikus, *Symmetry and Strain-Induced Effects in Semiconductors* (Wiley, New York, 1974).
- [10] H. Ehrenreich, Scattering of holes by phonons in germanium, *Phys. Rev.* **104**, 331 (1956).
- [11] G. L. Bir, E. Normantas, and G. E. Pikus, Galvanomagnetic effects in semiconductors with degenerate zones, *Sov. Phys. Solid State* **4**, 867 (1962).
- [12] B. K. Ridley, *Quantum Processes in Semiconductors*, 5th ed. (Oxford University Press, Oxford, 2013).
- [13] Z. Li, P. Graziosi, and N. Neophytou, Deformation potential extraction and computationally efficient mobility calculations in silicon from first principles, *Phys. Rev. B* **104**, 195201 (2021).
- [14] M. V. Fischetti and S. E. Laux, Band structure, deformation potentials, and carrier mobility in strained Si, Ge, and SiGe alloys, *J. Appl. Phys.* **80**, 2234 (1996).
- [15] F. L. Madarasz and F. Szmulowicz, Transition rates for acoustic-phonon-hole scattering in *p*-type silicon with nonparabolic bands, *Phys. Rev. B* **24**, 4611 (1981).
- [16] P. Lawaetz, Low-field mobility and galvanomagnetic properties of holes in germanium with phonon scattering, *Phys. Rev.* **174**, 867 (1968).
- [17] P. Zhao, L. Li, G. Chen, X. Guan, Y. Zhang, W. Meng, L. Zhao, K. Li, R. Jiang, S. Jia *et al.*, Structural evolution of low-dimensional metal oxide semiconductors under external stress, *J. Semicond.* **43**, 041105 (2022).
- [18] F. Giustino, Electron-phonon interactions from first principles, *Rev. Mod. Phys.* **89**, 015003 (2017).
- [19] S. Poncé, E. R. Margine, and F. Giustino, Towards predictive many-body calculations of phonon-limited carrier mobilities in semiconductors, *Phys. Rev. B* **97**, 121201(R) (2018).
- [20] W. Li, Electrical transport limited by electron-phonon coupling from Boltzmann transport equation: An *ab initio* study of Si, Al, and MoS₂, *Phys. Rev. B* **92**, 075405 (2015).
- [21] Q.-L. Yang, H.-X. Deng, S.-H. Wei, and J.-W. Luo, Group velocity matters for accurate prediction of phonon-limited carrier mobility, *Chin. Phys. B* **30**, 087201 (2021).
- [22] M. Huang, Z. Zheng, Z. Dai, X. Guo, S. Wang, L. Jiang, J. Wei, and S. Chen, DASP: Defect and dopant *ab-initio* simulation package, *J. Semicond.* **43**, 042101 (2022).
- [23] J.-J. Zhou, J. Park, I.-T. Lu, I. Maliyov, X. Tong, and M. Bernardi, PERTURBO: A software package for *ab initio* electron-phonon interactions, charge transport and ultrafast dynamics, *Comput. Phys. Commun.* **264**, 107970 (2021).
- [24] G. Brunin, H. P. C. Miranda, M. Giantomassi, M. Royo, M. Stengel, M. J. Verstraete, X. Gonze, G.-M. Rignanese, and G. Hautier, Phonon-limited electron mobility in Si, GaAs, and GaP with exact treatment of dynamical quadrupoles, *Phys. Rev. B* **102**, 094308 (2020).
- [25] J. Ma, A. S. Nissimagoudar, and W. Li, First-principles study of electron and hole mobilities of Si and GaAs, *Phys. Rev. B* **97**, 045201 (2018).
- [26] O. D. Restrepo, K. Varga, and S. T. Pantelides, First-principles calculations of electron mobilities in silicon: Phonon and Coulomb scattering, *Appl. Phys. Lett.* **94**, 212103 (2009).
- [27] P. Giannozzi, S. Baroni, N. Bonini, M. Calandra, R. Car, C. Cavazzoni, D. Ceresoli, G. L. Chiarotti, M. Cococcioni, I. Dabo *et al.*, QUANTUM ESPRESSO: A modular and open-source software project for quantum simulations of materials, *J. Phys.: Condens. Matter* **21**, 395502 (2009).
- [28] S. Poncé, E. R. Margine, C. Verdi, and F. Giustino, EPW: Electron-phonon coupling, transport and superconducting properties using maximally localized Wannier functions, *Comput. Phys. Commun.* **209**, 116 (2016).
- [29] S. Poncé, D. Jena, and F. Giustino, Hole mobility of strained GaN from first principles, *Phys. Rev. B* **100**, 085204 (2019).
- [30] F. Giustino, M. L. Cohen, and S. G. Louie, Electron-phonon interaction using Wannier functions, *Phys. Rev. B* **76**, 165108 (2007).
- [31] C. Canali, C. Jacoboni, F. Nava, G. Ottaviani, and A. Alberigi-Quaranta, Electron drift velocity in silicon, *Phys. Rev. B* **12**, 2265 (1975).
- [32] P. Norton, T. Braggins, and H. Levinstein, Impurity and lattice scattering parameters as determined from Hall and mobility analysis in *n*-type silicon, *Phys. Rev. B* **8**, 5632 (1973).
- [33] F. J. Morin and J. P. Maita, Electrical properties of silicon containing arsenic and boron, *Phys. Rev.* **96**, 28 (1954).
- [34] R. A. Logan and A. J. Peters, Impurity effects upon mobility in silicon, *J. Appl. Phys.* **31**, 122 (1960).
- [35] C. Jacoboni, C. Canali, G. Ottaviani, and A. Alberigi Quaranta, A review of some charge transport properties of silicon, *Solid-State Electron.* **20**, 77 (1977).
- [36] S. Adachi, *Properties of Group-IV, III-V and II-VI Semiconductors*, Wiley Series in Materials for Electronic and Optoelectronic Applications (John Wiley & Sons, Ltd, Chichester, 2006).
- [37] R. K. Willardson and A. C. Beer, *Transport Phenomena*, Semiconductors and Semimetals No. 10 (Academic Press, New York, 1975).
- [38] D. Bimberg, R. Blachnik, M. Cardona, P. J. Dean, T. Grave, G. Harbeke, K. Hübner, U. Kaufmann, W. Kress, O. Madelung *et al.*, *Physics of Group IV Elements and III-V Compounds*, edited by O. Madelung, Condensed Matter (Springer-Verlag, Berlin, 1982).
- [39] G. Brunin, H. P. C. Miranda, M. Giantomassi, M. Royo, M. Stengel, M. J. Verstraete, X. Gonze, G.-M. Rignanese, and G. Hautier, Electron-phonon beyond Fröhlich: Dynamical quadrupoles in polar and covalent solids, *Phys. Rev. Lett.* **125**, 136601 (2020).
- [40] V. A. Jhalani, J.-J. Zhou, J. Park, C. E. Dreyer, and M. Bernardi, Piezoelectric electron-phonon interaction from *ab initio* dynam-

- ical quadrupoles: Impact on charge transport in Wurtzite GaN, *Phys. Rev. Lett.* **125**, 136602 (2020).
- [41] J. Park, J.-J. Zhou, V. A. Jhalani, C. E. Dreyer, and M. Bernardi, Long-range quadrupole electron-phonon interaction from first principles, *Phys. Rev. B* **102**, 125203 (2020).
- [42] V. F. Gantmakher and I. B. Levinson, *Carrier Scattering in Metals and Semiconductors*, Modern problems in condensed matter sciences No. v. 19 (North-Holland, Amsterdam, 1987).
- [43] D. Long, Scattering of conduction electrons by lattice vibrations in silicon, *Phys. Rev.* **120**, 2024 (1960).
- [44] L. C. Lew Yan Voon and M. Willatzen, *The $\mathbf{k} \cdot \mathbf{p}$ Method: Electronic Properties of Semiconductors* (Springer, Dordrecht, 2009).
- [45] M. Lax and J. L. Birman, Intervalley scattering selection rules for Si and Ge, *Phys. Status Solidi B* **49**, K153 (1972).
- [46] M. Lax and J. J. Hopfield, Selection rules connecting different points in the Brillouin zone, *Phys. Rev.* **124**, 115 (1961).
- [47] H. W. Streitwolf, Intervalley scattering selection rules for Si and Ge, *Phys. Status Solidi B* **37**, K47 (1970).
- [48] S. Altmann and P. Herzig, *Point-Group Theory Tables* (Oxford University Press, Oxford, 1994).
- [49] J. Dresselhaus, *Group Theory: Application to the Physics of Condensed Matter* (Springer, Berlin, 2008).
- [50] W. A. Harrison, Scattering of electrons by lattice vibrations in nonpolar crystals, *Phys. Rev.* **104**, 1281 (1956).
- [51] R. J. Elliott and R. Loudon, Group theory of scattering processes in crystals, *J. Phys. Chem. Solids* **15**, 146 (1960).
- [52] N. Tandon, J. D. Albrecht, and L. R. Ram-Mohan, Electron-phonon interaction and scattering in Si and Ge: Implications for phonon engineering, *J. Appl. Phys.* **118**, 045713 (2015).
- [53] M. Lax, Subgroup techniques in crystal and molecular physics, *Phys. Rev.* **138**, A793 (1965).
- [54] D. K. Ferry, First-order optical and intervalley scattering in semiconductors, *Phys. Rev. B* **14**, 1605 (1976).
- [55] S. Y. Savrasov, D. Y. Savrasov, and O. K. Andersen, Linear-response calculations of electron-phonon interactions, *Phys. Rev. Lett.* **72**, 372 (1994).
- [56] S. V. Obukhov and V. G. Tyuterev, *Ab initio* calculation of the deformation potentials for intervalley phonons in silicon, *Phys. Solid State* **51**, 1110 (2009).
- [57] A. Blacha, H. Presting, and M. Cardona, Deformation potentials of $k = 0$ states of tetrahedral semiconductors, *Phys. Status Solidi B* **126**, 11 (1984).
- [58] M. Neuberger, *Handbook of Electronic Materials* (Springer US, Boston, 1971).
- [59] M. Tiersten, Acoustic-mode scattering mobility of holes in diamond type semiconductors, *J. Phys. Chem. Solids* **25**, 1151 (1964).
- [60] D. Kranzer, Mobility of holes of zinc-blende III–V and II–VI compounds, *Phys. Status Solidi A* **26**, 11 (1974).
- [61] M. Costato and L. Reggiani, Scattering probabilities for holes I. Deformation potential and ionized impurity scattering mechanisms, *Phys. Status Solidi B* **58**, 471 (1973).
- [62] J. D. Wiley, Valence-band deformation potentials for the III–V compounds, *Solid State Commun.* **8**, 1865 (1970).
- [63] P. Friedel, M. S. Hybertsen, and M. Schlüter, Local empirical pseudopotential approach to the optical properties of Si/Ge superlattices, *Phys. Rev. B* **39**, 7974 (1989).
- [64] C. Jacoboni and L. Reggiani, The Monte Carlo method for the solution of charge transport in semiconductors with applications to covalent materials, *Rev. Mod. Phys.* **55**, 645 (1983).
- [65] G. Ottaviani, L. Reggiani, C. Canali, F. Nava, and A. Alberigi-Quaranta, Hole drift velocity in silicon, *Phys. Rev. B* **12**, 3318 (1975).
- [66] J. Dewey and M. A. Osman, Monte Carlo study of hole transport in silicon, *J. Appl. Phys.* **74**, 3219 (1993).
- [67] K. Takeda, A. Taguchi, and M. Sakata, Valence-band parameters and hole mobility of Ge-Si alloys-theory, *J. Phys. C* **16**, 2237 (1983).
- [68] L. D. Laude, F. H. Pollak, and M. Cardona, Effects of uniaxial stress on the indirect exciton spectrum of silicon, *Phys. Rev. B* **3**, 2623 (1971).
- [69] M. M. Rieger and P. Vogl, Electronic-band parameters in strained $\text{Si}_{1-x}\text{Ge}_x$ alloys on $\text{Si}_{1-y}\text{Ge}_y$ substrates, *Phys. Rev. B* **48**, 14276 (1993).
- [70] C. Tserbak, H. M. Polatoglou, and G. Theodorou, Unified approach to the electronic structure of strained Si/Ge superlattices, *Phys. Rev. B* **47**, 7104 (1993).
- [71] C. G. Van de Walle and R. M. Martin, Theoretical calculations of heterojunction discontinuities in the Si/Ge system, *Phys. Rev. B* **34**, 5621 (1986).
- [72] M. Cardona and F. H. Pollak, Energy-band structure of germanium and silicon: The $\mathbf{k} \cdot \mathbf{p}$ method, *Phys. Rev.* **142**, 530 (1966).
- [73] Q. L. Yang, H. X. Deng, S. H. Wei, S. S. Li, and J. W. Luo, Materials design principles towards high hole mobility learning from an abnormally low hole mobility of silicon, [arXiv:2011.02262](https://arxiv.org/abs/2011.02262).
- [74] V. Palankovski, Simulation of Heterojunction Bipolar Transistors, Ph.D. thesis, Vienna University of Technology, 2000.
- [75] nextnano documentation, <https://www.nextnano.com/documentation/index.html>.
- [76] S. M. Sze and K. K. Ng, *Physics of Semiconductor Devices*, 1st ed. (Wiley, Hoboken, 2006).
- [77] Sentaurus Device: Technology Computer Aided Design (TCAD), Synopsys, <https://www.synopsys.com/manufacturing/tcad/device-simulation/sentaurus-device.html>.